the plant journal

SEB SOCIETY FOR EXPERIMENTAL BIOLOGY

The Plant Journal (2024) doi: 10.1111/tpj.16651

Structural and biochemical characterization of Arabidopsis alcohol dehydrogenases reveals distinct functional properties but similar redox sensitivity

Maria Meloni[1,†], Jacopo Rossi[1,†], Silvia Fanti[2,†], Giacomo Carloni[2], Daniele Tedesco[3], Patrick Treffon[4], Luca Piccinini[5,6], Giuseppe Falini[2], Paolo Trost[1], Elizabeth Vierling[4], Francesco Licausi[7], Beatrice Giuntoli[5,6], Francesco Musiani[1,*], Simona Fermani[2,8,*] and Mirko Zaffagnini[1,*]

[1]*Department of Pharmacy and Biotechnology, University of Bologna, 40126 Bologna, Italy,*
[2]*Department of Chemistry "G. Ciamician", University of Bologna, 40126 Bologna, Italy,*
[3]*Institute for Organic Synthesis and Photoreactivity (ISOF), National Research Council of Italy (CNR), 40129 Bologna, Italy,*
[4]*Department of Biochemistry and Molecular Biology, University of Massachusetts Amherst, Amherst, Massachusetts, USA,*
[5]*Department of Biology, University of Pisa, Pisa 56127, Italy,*
[6]*Center for Plant Sciences, Scuola Superiore Sant'Anna, Pisa 56124, Italy,*
[7]*Department of Plant Sciences, University of Oxford, Oxford, UK, and*
[8]*Interdepartmental Centre for Industrial Research Health Sciences & Technologies, University of Bologna, 40064 Bologna, Italy*

Received 20 October 2023; revised 7 January 2024; accepted 18 January 2024.
*For correspondence (e-mail francesco.musiani@unibo.it, simona.fermani@unibo.it, mirko.zaffagnini3@unibo.it).
†Equal contribution.

SUMMARY

Alcohol dehydrogenases (ADHs) are a group of zinc-binding enzymes belonging to the medium-length dehydrogenase/reductase (MDR) protein superfamily. In plants, these enzymes fulfill important functions involving the reduction of toxic aldehydes to the corresponding alcohols (as well as catalyzing the reverse reaction, i.e., alcohol oxidation; ADH1) and the reduction of nitrosoglutathione (GSNO; ADH2/GSNOR). We investigated and compared the structural and biochemical properties of ADH1 and GSNOR from *Arabidopsis thaliana*. We expressed and purified ADH1 and GSNOR and determined two new structures, NADH-ADH1 and apo-GSNOR, thus completing the structural landscape of Arabidopsis ADHs in both apo- and holoforms. A structural comparison of these Arabidopsis ADHs revealed a high sequence conservation (59% identity) and a similar fold. In contrast, a striking dissimilarity was observed in the catalytic cavity supporting substrate specificity and accommodation. Consistently, ADH1 and GSNOR showed strict specificity for their substrates (ethanol and GSNO, respectively), although both enzymes had the ability to oxidize long-chain alcohols, with ADH1 performing better than GSNOR. Both enzymes contain a high number of cysteines (12 and 15 out of 379 residues for ADH1 and GSNOR, respectively) and showed a significant and similar responsivity to thiol-oxidizing agents, indicating that redox modifications may constitute a mechanism for controlling enzyme activity under both optimal growth and stress conditions.

Keywords: alcohol dehydrogenase, 3D structure, cysteine, thiol oxidation, zinc ion, redox sensitivity, ethanol, nitrosoglutathione, *Arabidopsis thaliana*.

INTRODUCTION

Alcohol dehydrogenases (ADHs) comprise several classes of metal-containing enzymes belonging to the protein superfamily of medium-length dehydrogenase/reductases (MDRs) (Persson et al., 2008). ADHs are mostly known in plants for their participation in fermentative metabolism, in which they catalyze the NADH-dependent conversion of acetaldehyde (MeCHO) to ethanol (EtOH) (Strommer, 2011). This reaction detoxifies MeCHO and sustains the glycolytic flux by NAD^+ regeneration under conditions of impaired mitochondrial respiration (Antonio et al., 2016; Bui et al., 2019; Loreti et al., 2016). In addition, ADHs are able to catalyze the reverse NAD^+-dependent conversion of alcohols to aldehydes (e.g., EtOH to MeCHO) (Strommer, 2011). Among the enzymes belonging to the MDR superfamily, the class III ADH family includes nitrosoglutathione reductase

(GSNOR). GSNOR is involved in the detoxification of toxic aldehyde compounds (Fliegmann & Sandermann, 1997), but is primarily implicated in the degradation of S-nitrosoglutathione (GSNO) (Liu et al., 2001), the most important NO-releasing compound in both plant and non-plant cells (Broniowska et al., 2013; Zaffagnini, De Mia, et al., 2016; Zaffagnini, Fermani, et al., 2019). As a relatively stable molecule, GSNO can react with cysteine thiols in proteins in a reaction called S-nitrosylation (or S-nitrosation), which plays a fundamental role in modulating protein function and structure (Huang, Huo, et al., 2019; Zaffagnini, De Mia, et al., 2016).

When considering the relative content of the different proteinogenic amino acids, cysteine (Cys) is one of the least abundant residues. Nevertheless, Cys plays a key role in enzyme function and protein structure stabilization (Paulsen & Carroll, 2013; Poole, 2015). Cys can form structural disulfide bonds that are fundamental for the proper folding of a wide range of proteins (Dupuis et al., 2020; Marshall et al., 2010; Trivedi et al., 2009). When located in the active site of an enzyme, Cys residues can fulfill a catalytic function by forming covalent bonds with the substrate, as observed for thioredoxins, glutaredoxins, peroxiredoxins, and glyceraldehyde-3-phosphate dehydrogenases (Zaffagnini, Fermani, et al., 2019). Besides functioning in enzyme activity and folding, Cys can also coordinate metal ions (Krzywoszynska et al., 2020). Zinc ions are one of the most abundant biologically relevant transition metals, typically coordinated by four ligands in a tetrahedral geometry. Cys residues in combination with histidine (most favored) and negatively charged residues (e.g., aspartate and glutamate) are typically involved in the coordination of zinc ions that can serve both structural and catalytic functions (Pace & Weerapana, 2014). In this regard, ADHs represent a textbook example since they contain two zinc ions, coordinated either by 4 Cys or by 2 Cys coupled to a histidine and a glutamate that in some cases is replaced by a water molecule (Lindermayr, 2017; Strommer, 2011).

Depending on reactivity and microenvironment, Cys residues can undergo a wide range of redox post-translational modifications (PTMs) that are able to modulate protein function or alter structural conformations (Mattioli et al., 2022; Trost et al., 2017; Zaffagnini, De Mia, et al., 2016; Zaffagnini, Fermani, et al., 2019). This property makes Cys residues exceptionally important for redox homeostasis in plant cells and cysteines are considered the primary sensor of reactive oxygen and nitrogen species (ROS and RNS, respectively). Numerous proteomic-based studies have identified hundreds of plant proteins susceptible to thiol-based redox modifications ([Zaffagnini, Fermani, et al., 2019] and references therein). Among metabolism-related proteins, ADH1 and GSNOR were recently identified in *Arabidopsis thaliana* as putative targets of S-sulfenylation (i.e., Cys hydroxylation) both under control conditions and after exposure to hydrogen peroxide (H_2O_2) (Huang, Willems, et al., 2019; Wei et al., 2020). In addition, both proteins showed sensitivity toward S-nitrosylation (Fares et al., 2011; Frungillo et al., 2014; Guerra et al., 2016; Zhan et al., 2018; Zhang et al., 2020), while other redox modifications, such as S-glutathionylation and thioredoxin-mediated dithiol/disulfide interchanges, specifically target ADH1 (Dixon et al., 2005; Yamazaki et al., 2004).

Here, we first determined new crystal structures of *Arabidopsis thaliana* ADH1 complexed with NADH (NADH-ADH1) and of GSNOR in the apo-form (apo-GSNOR) in order to broaden our knowledge of the structural landscape of ADHs and to conduct an in-depth structural comparison between the different apo- and holo- forms (NAD^+ and NADH structures) (Table 1). Then, we performed a kinetic analysis to establish specificity toward the enzyme's respective substrates as well as alternative substrates such as long-chain alcohols. The two enzymes exhibit nearly an identical fold but have striking differences in catalytic behavior and catalytic-related structural elements. We further examined the content, conservation, and accessibility of cysteine thiols in the two enzymes, and evaluated their redox sensitivity in the presence of various thiol oxidizing agents. We evidenced similar and prominent redox responsivity of ADHs to thiol switching mechanisms with concomitant destabilization of zinc ion coordination, suggesting that cysteine-based modifications may constitute a mechanism for controlling their activity under physiological conditions and in response to oxidative stress.

Table 1 3D-structures for *A. thaliana* ADH1 and GSNOR in the Protein Data Bank

	PDB ID	Resolution (Å)	Asymmetric unit	Ligand	Oligomeric state	References
ADH1	4RQT	2.30	Monomer	Acetate	Dimer	(Chen et al., 2014)
	4RQU	2.50	Dimer	NAD^+[a]	Dimer	(Chen et al., 2014)
	8CON	1.64	Monomer	NADH	Dimer	(this work)
GSNOR	4JJI[b]	1.80	Dimer	NAD^+	Dimer	–
	3UKO[b]	1.40	Dimer	NADH	Dimer	–
	8CO4	1.90	Dimer of dimers	–	Dimer	(this work)

[a]The cofactor is found only in one chain of the dimer (chain B).
[b]Crystal structures deposited in the Protein Data Bank.

RESULTS

Arabidopsis ADH1 and GSNOR share a similar fold with identical domain organization

To gain a better understanding of the structural properties and to identify differences between Arabidopsis ADH1 and GSNOR, we expressed and purified both proteins and determined two new structures, NADH-ADH1 and apo-GSNOR. These new structures now provide a complete set of Arabidopsis ADHs in both apo- and holo-forms (Table 1). The extensive similarity of the two proteins is first observed by comparative analysis of their primary sequences, both of which comprise 379 amino acids, along with their secondary structures. Despite their different physiological roles, ADH1 and GSNOR share ~59% sequence identity and exhibit a nearly complete conservation of secondary structure composition (Figure S1). Based on the complete set of 3D structures reported (Table 1), ADH1 and GSNOR are both homodimers with a similar tertiary structure (Figure 1a,b and Table 1). According to the CATH classification (Orengo et al., 1997), each monomer is composed of two domains (Figure 1a,b). The catalytic domain comprises the N-terminal portion and the C-terminal tail of the protein (residues 1–177 and 327–379) and is formed by 11 β-strands and 10 or 11 helices for ADH1 and GSNOR, respectively, with the additional helix inserted between β5 and β6 in GSNOR (Figure 1c,d). The cofactor binding domain has a typical Rossman fold (residues 178–326), formed by a six-strand parallel β-sheet surrounded by seven helices (Figure 1c,d). The interaction between the cofactor binding domains of the two subunits allows the formation of the quaternary assembly, while the catalytic domains are located in the distal portion of the ADH structures (Figure 1a,b). The cofactor binding domain hosts NAD^+/NADH cofactor in a wide pocket at the interface between the two domains (Figure 1a,b). The conformation of the cofactor is very similar in all monomers, except for chain B of the NAD^+-GSNOR structure (PDB ID 4JJI) where the nicotinamide-ribose moiety is rotated by about 90° (Figure S2).

Structural and catalytic zinc ions in Arabidopsis ADHs

Arabidopsis ADHs contain two zinc ions having either structural or catalytic role (Chen et al., 2015; Xu et al., 2013), and the effective content of zinc atoms was determined for the purified recombinant proteins using the 4-(2-pyridylazo) resorcinol (PAR) assay. As expected, the number of zinc ions released from ADH1 and GSNOR are 1.94 ± 0.14 and 2.05 ± 0.13, respectively. In the available structures (Table 1), the structural zinc ion is located in a loop at ca. 25 Å from the active site (Figure 1a,b) and it is coordinated by four cysteines (Cys99, Cys102, Cys105, and Cys113 in both ADHs; Figure 2a) in a slightly distorted tetrahedral geometry (root mean square deviations (RMSDs) 0.125–0.237 Å with respect to the ideal tetrahedral geometry; Figure S3). In contrast, the catalytic zinc ion, which is involved in substrate stabilization/activation, shows a variable number of ligands and coordination geometry (Figures 2b,c; Figure S4) as is typical for zinc ions exhibiting catalytic functions (Permyakov, 2021). In all structures, the catalytic zinc ion is bound to Cys47, His69, and Cys177, while there is variability of the fourth ligand (Glu70, water or substrate), and the fifth ligand, when present, is always a water molecule (Figure S4). However, in the NADH-ADH1/GSNOR structures, the catalytic zinc ion is found in a distorted tetrahedral coordination geometry with Glu70 directly bound to the metal ion (Figure 2b; Figure S4).

Structural comparison of ADH1 and GSNOR in apo- and holo-forms

In order to highlight significant structural differences between the two enzymes, a comparative analysis was performed by superposing the available 3D structures (Table 1) and calculating the RMSDs of the positions of the C_α atoms per residue and as the average value of the whole protein chain (Figure 3; Figure S5 and Tables S1-S3).

The monomers of the apo- and NAD(H)-ADH1 structures are similar having an average RMSD (<RMSD>) of 0.69 ± 0.15 Å, slightly higher than that obtained from the superposition of the apo- and NAD(H)-GSNOR structures (<RMSD> = 0.58 ± 0.16 Å) (Table S3). This trend is paralleled by the average RMSD values for the dimers (<RMSD> = 1.13 ± 0.18 Å for ADH1 and < RMSD> = 0.81 ± 0.27 Å for GSNOR; Tables S3). Despite the low RMSD values, the superposition of ADH1 monomers (apo- and NAD(H) forms) shows structural deviations especially in the cofactor binding domain with RMSD values per monomer up to 4 Å (Figure S5a,c). In contrast, these differences are not observed among monomers of apo- and holo-GSNOR (Figure S5b,d). These observations argue that there is conformational variability among different ADH1 forms compared with GSNOR, which appears to be more rigid.

The superposition of ADH1 and GSNOR (i.e., apo-ADH1 vs apo-GSNOR and NAD(H)-ADH1 vs NAD(H)-GSNO) reveals higher structural deviations with RMSD values ranging from 0.93 Å to 1.52 Å for monomers and 1.58 Å to 2.43 Å for dimers (Table S1–S3). Major differences are observed in the non-conserved regions that delimit the entrance to the catalytic cavity and that form the cavity itself, including the loop 55–69 following helix α1, residues 115–132, and residues 297–303 (Figure 3; Figure S6). Helix α1 and residues 297–303 are also involved in setting in place the nicotinamide moiety of the cofactor. Residues 115–132, which have RMSD values per residue higher than 4 Å (Figure 3b,d,f), acquire a different conformation in the two enzymes, forming a turn/loop in ADH1 and a helix/loop in GSNOR (Figure 3a,c,e; Figure S1). Moreover, in ADH1

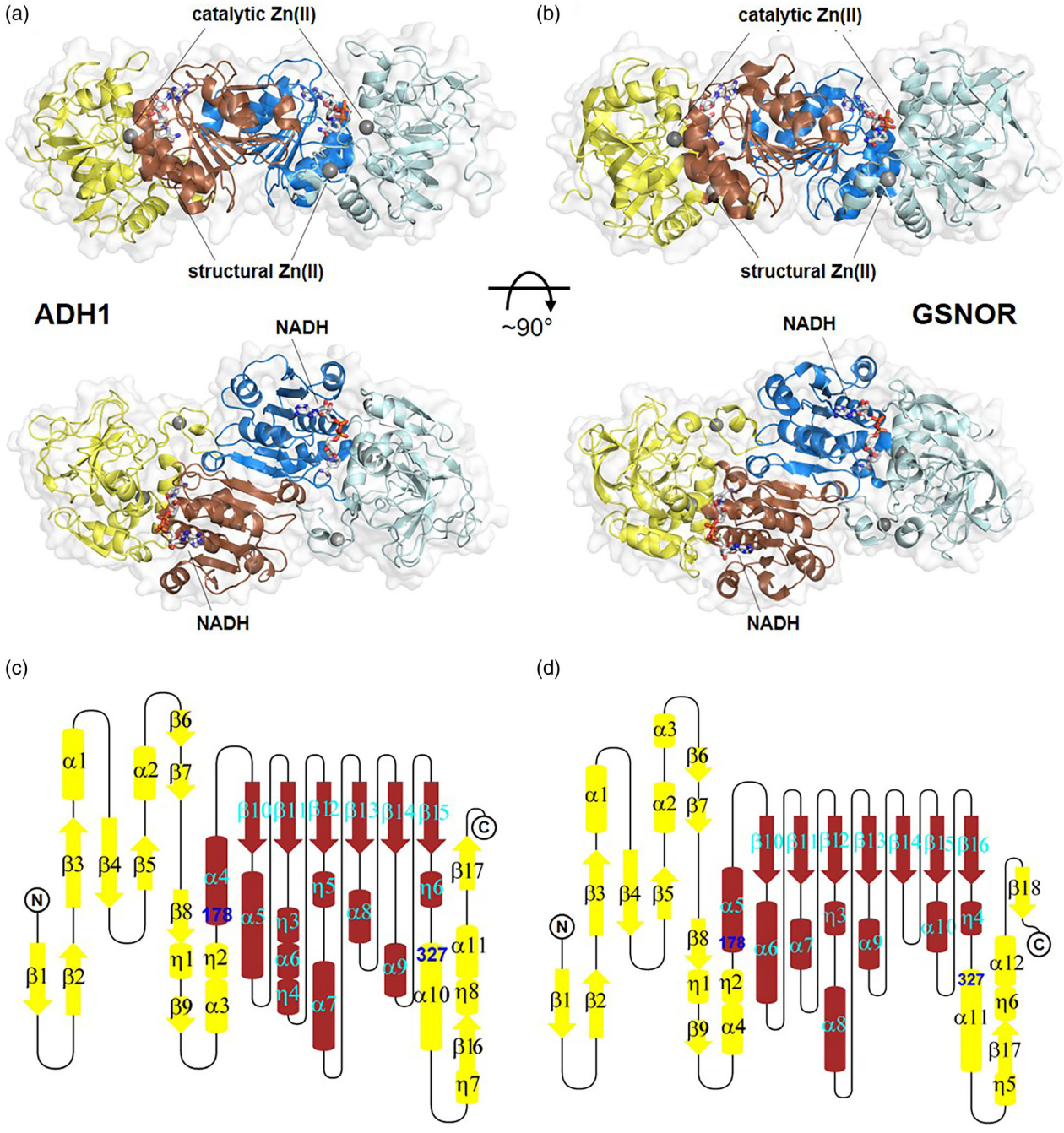

Figure 1. Overview of ADH1 and GSNOR structures.
Cartoon and surface representation of structures of ADH1 (PDB ID: 8CON) (a) and GSNOR (PDB ID: 3UKO) (b) in the presence of NADH. In the bottom panels, the structure is rotated by 90° degrees around the horizontal axis with respect to the upper panels. The two monomers of the dimers are colored yellow/orange (ADH1) and aquamarine/blue (GSNOR). In each monomer, the catalytic domain is shown in lighter colors (yellow and aquamarine) with respect to the cofactor binding domain (orange and blue). The surface is shown in white. Zinc ions are indicated as Zn(II) (see Figure 2 and related text for further details). Panels (c) and (d) are topology diagrams of ADH1 and GSNOR, respectively. The catalytic domain (yellow) comprises residues 1–177 and 327–379 and is composed of 11 β-strands and 10 or 11 helices for ADH1 and GSNOR, respectively. The cofactor binding domain (dark red) comprises residues 178–326 and is composed of a six-strand parallel β-sheet and seven helices. Residues 178 and 327 are highlighted in blue.

access to the catalytic cavity appears to be narrowed compared to GSNOR.

Notwithstanding the differences in cofactor binding domain and catalytic cavity, the residues involved in cofactor stabilization are almost entirely conserved (Figure 4; Table S4). Minor differences, which do not alter the cofactor-protein interaction network between the two enzymes, correspond to Ala205, Arg231, and Thr272 in

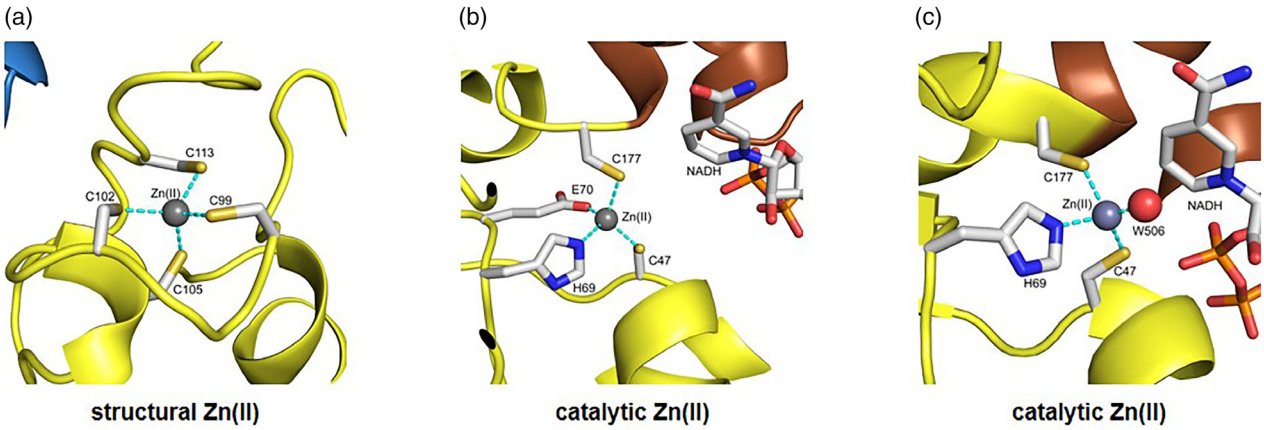

Figure 2. Coordination sites of zinc ions in Arabidopsis ADHs.
(a) Representation of the coordination environment of the structural zinc ion in ADHs (from NADH-ADH1 structure, PDB ID: 8CON). The metal-coordination bonds are reported as dashed cyan lines. (b) and (c) Representation of the coordination environment of two catalytic zinc ions in ADHs from NADH-ADH1 structure, PDB ID: 8CON and NAD + -ADH1 structure chain B, PDB ID: 4RQU, respectively. The metal coordination bonds are reported as dashed cyan lines. Zinc ions are represented as gray spheres, water molecules as red sphere while the NADH cofactor and protein residues are shown in sticks colored according to the atom type (C. light gray; O, red; N, blue; S, yellow; P, orange).

ADH1, replaced by Val205, Lys231, and Ile272 in GSNOR (Figure 4; Table S4). Conversely, substitution of ADH1 Phe95 for Tyr95 in GSNOR results in an additional interaction (Figure 4b; Table S4). The adenine ring of NAD(H) in ADH1 structures is stabilized through a π-staking interaction with Phe227 and the methyl group of Thr272 and Ala277 (Figure 4a). These residues are not conserved in GSNOR and Van der Walls interactions with Ile227, Ile272, and Val277 stabilize the adenine (Figure 4b). The stabilization of the nicotinamide ring is conserved in both enzymes and involves Val206, Val297, and the methyl group of Thr181 (Figure 4a,b).

Positioning of zinc ions was analyzed by structural superposition of the ADH structures. While the position of the structural zinc is similar in all apo- and NAD(H)-forms of ADH1 and GSNOR structures, the catalytic zinc ion assumes slightly variable positions, especially in the case of NAD^+-structures (Figure 3c; Figure S5a,b). In NADH-structures of both enzymes, the distance of the catalytic zinc ion from the nicotinamide ring (C5N atom) of NAD(H) ranges between 5.0 and 5.9 Å, while it decreases to 3.2 Å in NAD^+-AtADH1 structure (Figure 3c) and increases to 7.8 Å in NAD^+-AtGSNOR structure (chain B) (Figure S2).

Overall, this comparative analysis of the different forms of the two enzymes highlights that despite their structural similarity, specific structural differences are observed in the regions delimiting the shape and size of the catalytic cavity.

ADH1 and GSNOR exhibit non-redundant catalytic properties

To compare the catalytic behavior of ADH1 and GSNOR, we first determined the pH optimum of their respective activities: NAD^+-dependent oxidation of EtOH for ADH1, and NADH-dependent degradation of GSNO for GSNOR. The highest rate of ADH1 for EtOH oxidation was measured at pH 10.0, while GSNOR efficiently degraded GSNO between pH 7.9 and 9.0 (Figure S7). At their optimal pH (pH 10 and 7.9 for ADH1 and GSNOR, respectively), the two enzymes possess similar specific activities (Figure 5a) with values comparable to paralogs from other organisms (Chang et al., 2021). We then examined whether one protein could act on the other's substrate. The oxidation of ethanol was measured at pH 10, and the degradation of GSNO at pH 7.9. As shown in Figure 5a, ADH1 cannot catalyze NADH-dependent degradation of GSNO, and GSNOR cannot use EtOH as a substrate (i.e., undetectable activities). These data indicate that these similar proteins are highly specific for their respective substrates and associated physiological roles.

To discern structural differences that might be responsible for their divergent catalytic abilities, the shape, and volume of their catalytic cavity were examined. The volume of the internal cavities of each protein monomer without cofactor was calculated using the method described by Damborský and co-workers (Chovancova et al., 2012) that makes use of two probe spheres of different radius. Representative catalytic cavities of ADH1 and GSNOR are depicted in Figure 5b,c, while the complete set of calculated cavities is described in Figure S8. The calculated cavities of GSNOR are more than twice as large as those of ADH1, with an average volume of 3722 ± 395 $Å^3$ and 1567 ± 122 $Å^3$, respectively. Thus, GSNOR presents a much larger substrate-binding pocket, presumably linked to the ability to better accommodate larger substrates (e.g., GSNO). Consistently, the number of residues involved in the formation of catalytic cavity is higher for GSNOR (93 residues) compared to ADH1 (53 residues)

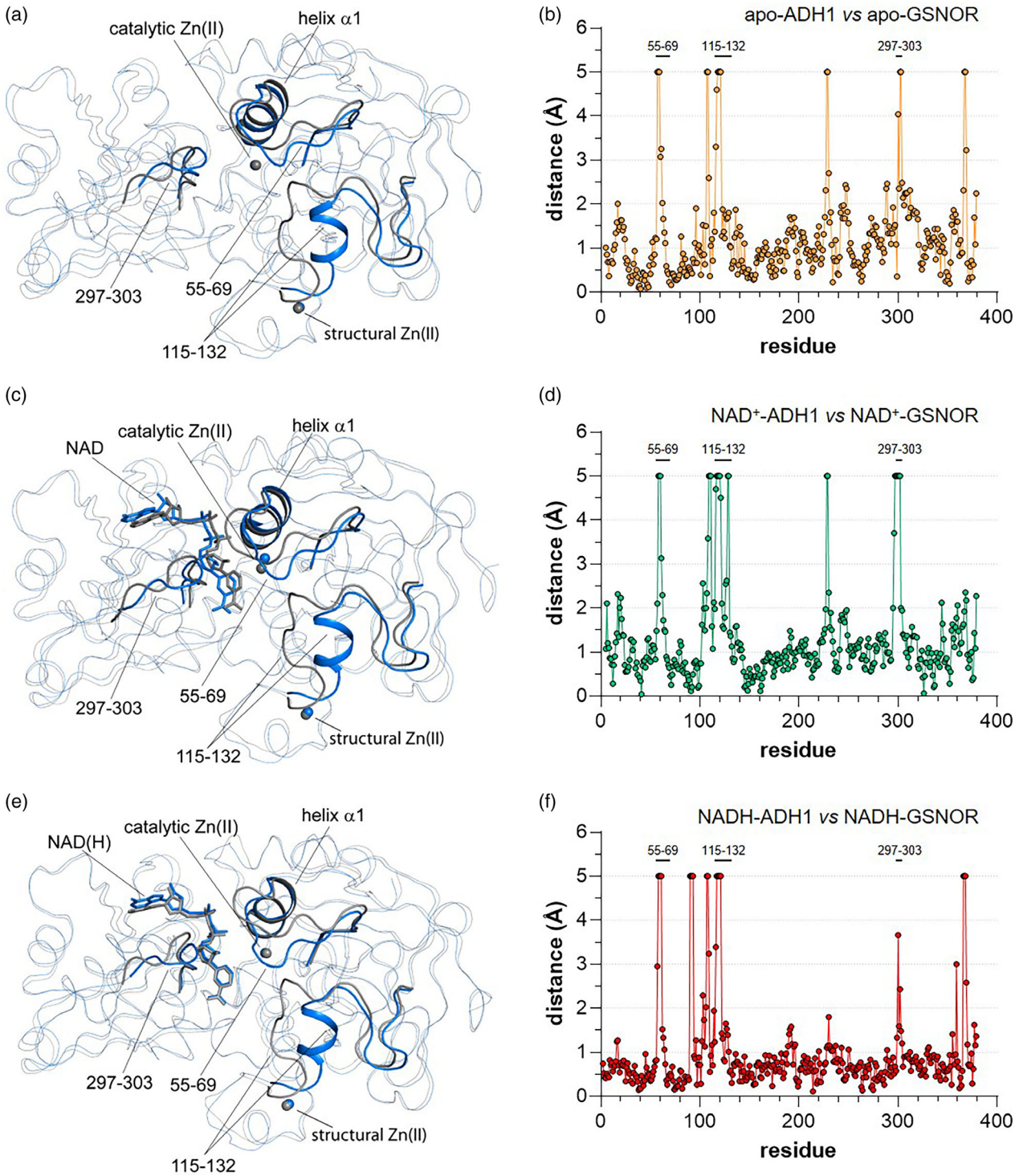

Figure 3. ADH1 and GSNOR structural superpositions.
Left panels show the C_α atoms superposition of ADH1 (gray) and GSNOR (light blue) monomers in apo-form (a), NAD^+-form (c), and NADH-form (e). The protein backbone is reported as ribbon, zinc ion as sphere, and cofactor as sticks. The protein portions delimiting the catalytic cavity and showing major differences are indicated. Right panels report the RMSD values per residue obtained from the C_α atoms superposition of ADH1 and GSNOR monomers in apo-form (b, orange closed circles), NAD^+-form (d, green closed circles), and NADH-form (f, red closed circles). RMSD values equal to or greater than 5 Å are set at 5 Å for clarity.

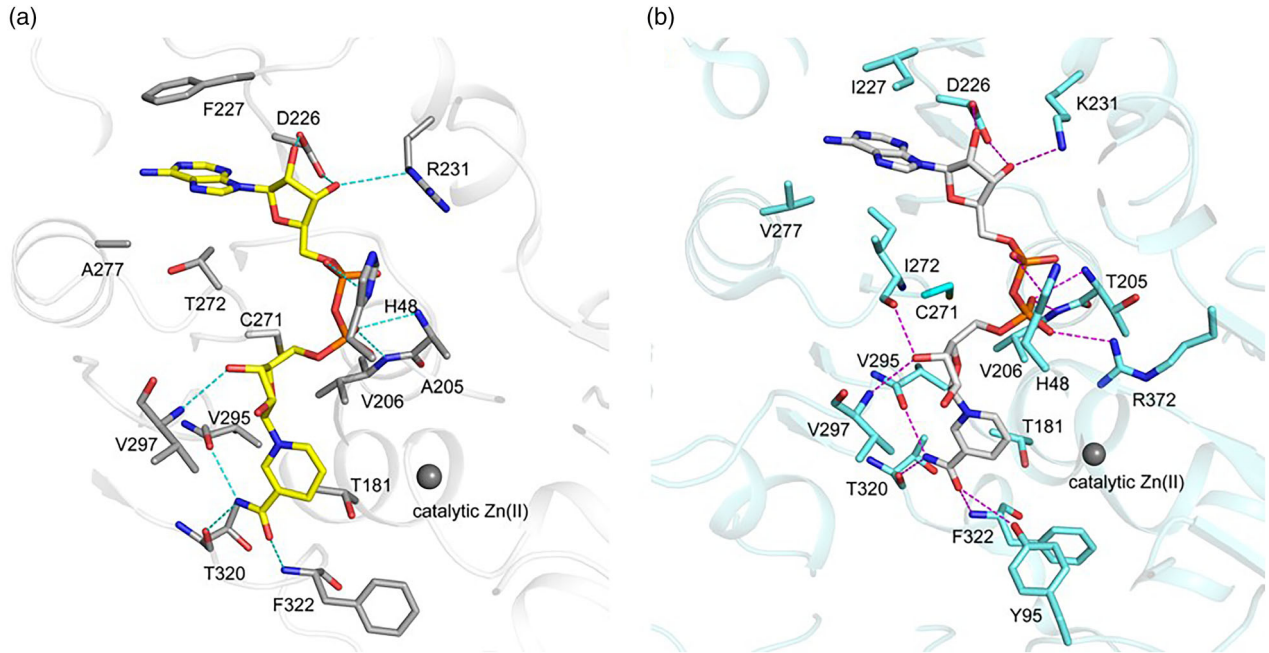

Figure 4. Cofactor-protein interactions in Arabidopsis ADHs.
Interactions between NADH and protein residues in ADH1 (a) and GSNOR (b). The cofactor and the protein residues are shown as sticks, the catalytic zinc ion is shown as a gray sphere, and the hydrogen-bond interactions (distance ≤3.6 Å) are indicated as dashed lines. The corresponding distance values observed in different ADH1 and GSNOR monomers are reported in Table S5. Residues forming Van der Walls interactions with the adenine and nicotinamide rings are also shown.

(Figure S6). In addition, those residues present in both proteins are only partially conserved (47% sequence identity) (Figure S6), indicating that specific residues in the active site contribute to the observed substrate selectivity of these enzymes.

Catalytic activity of ADH1 and GSNOR with long-chain alcohols

As highlighted in previous studies, plant ADHs can catalyze the reduction of various long-chain alcohols (Achkor et al., 2003; Kubienova et al., 2013; Strommer, 2011). Thus, we examined whether ADH1 and GSNOR could use octanol, geraniol, and cinnamyl alcohol as substrates. As shown in Figure 5d,e, both enzymes catalyzed the NAD^+-dependent oxidation of long-chain alcohols at pH 10, though exhibiting largely different specific activities. In particular, ADH1 showed maximal activity in the presence of cinnamyl alcohol (32.81 μmol min^{-1} mg^{-1}), which was ~22% of that measured with EtOH (Figure 5d). Similarly, GSNOR preferentially used cinnamyl alcohol but with a sevenfold lower specific activity compared to ADH1 (4.54 μmol min^{-1} mg^{-1}; Figure 5e). When we measured the NAD^+-dependent oxidation of octanol, the activity of GSNOR was very low (0.39 μmol min^{-1} mg^{-1}), while ADH1 catalyzed the reaction with a specific activity of 11.35 μmol min^{-1} mg^{-1}, a value that corresponds to ~8% of EtOH-dependent activity (Figure 5d,e). Almost identical activities were measured in the presence of geraniol (2.82 and 3.03 μmol min^{-1} mg^{-1} for ADH1 and GSNOR, respectively; Figure 5d,e). For all long-chain alcohols, enzyme activities drastically dropped when monitored at pH 7.9, and in some cases, catalysis was almost undetectable (Figure 5d,e), suggesting that NAD^+-dependent oxidizing reactions are strongly favored at alkaline conditions. In sum, these results indicate that these two functionally divergent enzymes share the catalytic ability to oxidize long-chain alcohols, albeit with different catalytic capacities. Thus, the conformation of the active sites in the two ADHs appears adapted to the specific recognition of EtOH and GSNO but has structural similarities that allow both enzymes to use long-chain alcohols as substrates.

Cysteine conservation, accessibility, and reactivity in Arabidopsis ADHs

ADH1 and GSNOR are cysteine-rich proteins containing 12 and 15 Cys residues, respectively (Figure S6). Among protein cysteines, 11 are fully conserved including Cys10, Cys173, Cys271, Cys284, Cys373, and the 6 invariable zinc-coordinating residues (Cys47 and Cys177 for the catalytic zinc ion, and Cys99, Cys102, Cys105, and Cys113 for the structural zinc ion; Figures S6), while Cys243 and Cys65/Cys94/Cys285/Cys370 are exclusively found in ADH1 and GSNOR, respectively (Figure S6).

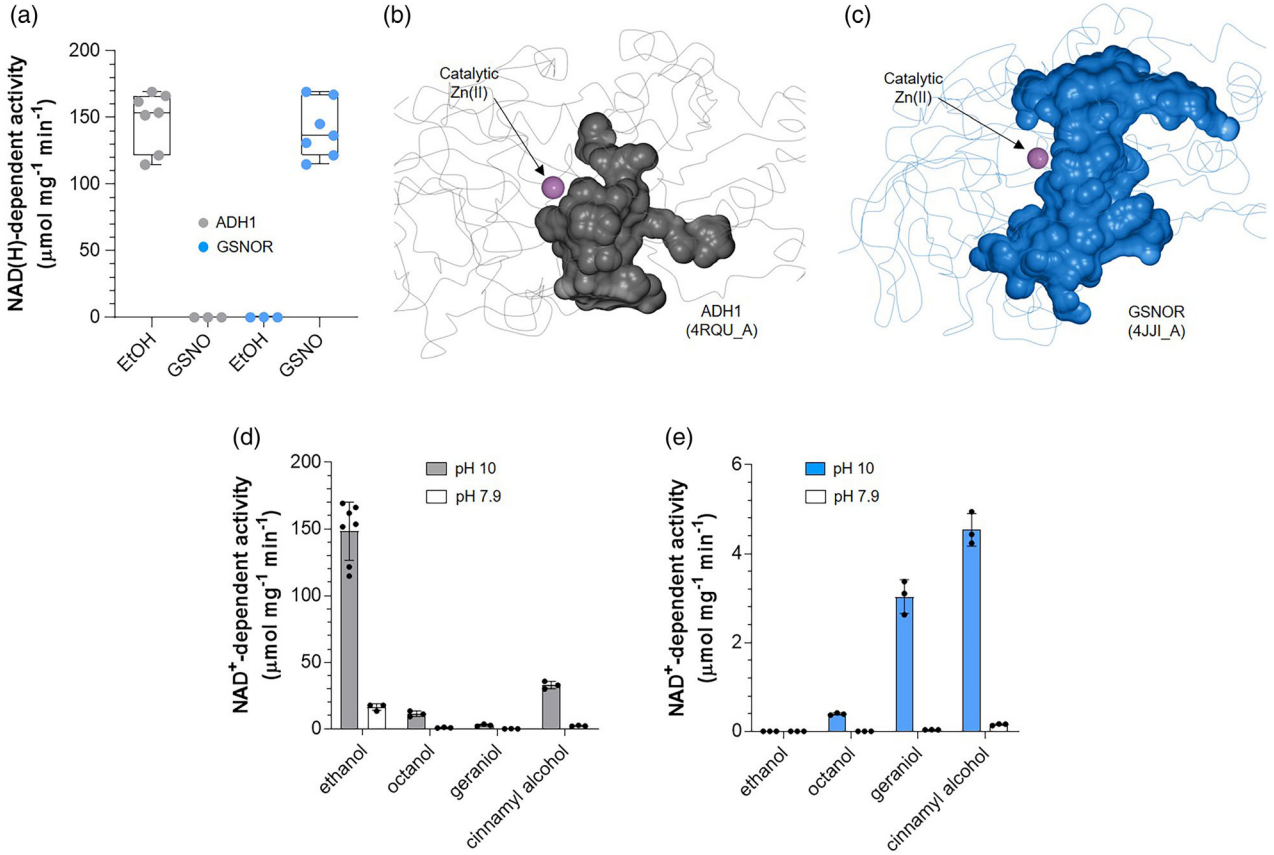

Figure 5. Analysis of kinetic properties of ADH1 and GSNOR.
(a) Specific activities of ADH1 (gray closed circles) and GSNOR (blue closed circles) measured in the presence of 50 mM EtOH and 2 mM NAD^+ (EtOH oxidation, EtOH) or 0.4 mM GSNO and 0.2 mM NADH (GSNO degradation, GSNO). For both enzymes, activity measurements for EtOH oxidation and GSNO degradation were carried out at pH 10 and 7.9, respectively. The box plots are built on the basis of seven biological replicates. Solvent excluded surface of the internal cavity calculated for two representative ADH1 (b) and GSNOR (c) monomers. The protein backbone is represented by a thick ribbon and the catalytic zinc ion is represented by a violet sphere.
(d) Specific activities of ADH1 in the presence of ethanol or different long-chain alcohols (cinnamyl alcohol, geraniol, and octanol). Activities were determined at pH 10 (gray bars) and 7.9 (white bars). Data are represented as mean ± SD (n = 3).
(e) Specific activities of GSNOR in the presence of different long chain alcohols (cinnamyl alcohol, geraniol, and octanol). Activities were determined at pH 10 (blue bars) and 7.9 (white bars). Data are represented as mean ± SD (n = 3). For panels D and E, long-chain alcohols were used at 5 mM to ensure their solubility in water.

To establish the number of solvent-exposed thiols and their position, we calculated the accessible surface area (ASA) of the entire residue and the Sγ atoms of cysteines (Table S5). ASA calculation revealed that ADH1 and GSNOR contain 4 and 7 cysteines, respectively, showing no or very low solvent accessibility (Cys10, 173, 284, and 373 for ADH1; Cys10, 65, 94, 173, 284, 285, and 372 for GSNOR; Table S5). Conversely, some cysteine residues stabilizing the structural and catalytic zinc ions are exposed to solvent, although their Sγ atoms show limited accessibility (Table S5). Similarly, Cys271 in the apo-forms of both enzymes, Cys243 in apo-ADH1, and Cys370 in apo-GSNOR show ASA values that range between 14 and 40 $Å^2$, while the accessibility of their thiol group is zero or significantly lower (Table S5). Interestingly, in both enzymes, Cys271 becomes buried when the cofactor (NADH or NAD^+) is bound as the phosphate group and ribose of the nicotinamide moiety are located in front of it (Figure 4), reducing its exposure to the solvent (Table S5). Cofactor binding significantly reduces the accessibility of other Cys in GSNOR, namely Cys370 and zinc-coordinating cysteine residues (Cys47, Cys102, and Cys177) (Table S5). In summary, the number of solvent-exposed cysteine residues is five for ADH1 (Cys99, 102, 105, 243, and 271) and seven for GSNOR (Cys47, 99, 102, 105, 177, 271, and 370) (Table S5).

The number of accessible cysteine thiols in ADH1 and GSNOR was further investigated by thiol titration using Ellman's reagent (5,5′-dithiobis(2-nitrobenzoic acid), DTNB). This analysis showed that each monomer of ADH1 and GSNOR contains ~2 accessible cysteine thiols (2.04 ± 0.19 and 2.02 ± 0.41 for ADH1 and GSNOR, respectively). Almost identical values were found for the pre-reduced

ADH1 and GSNOR, being 2.22 ± 0.14 and 2.19 ± 0.25, respectively. To evaluate whether derivatization of accessible thiols had an effect on enzyme activities, we examined the redox response of ADH1 and GSNOR to DTNB and the alkylating agent NEM. Although both compounds are reactive toward accessible cysteine residues, DTNB causes reversible thiol modifications (i.e., disulfide bonds), while NEM binds irreversibly. As shown in Figure 6a, both

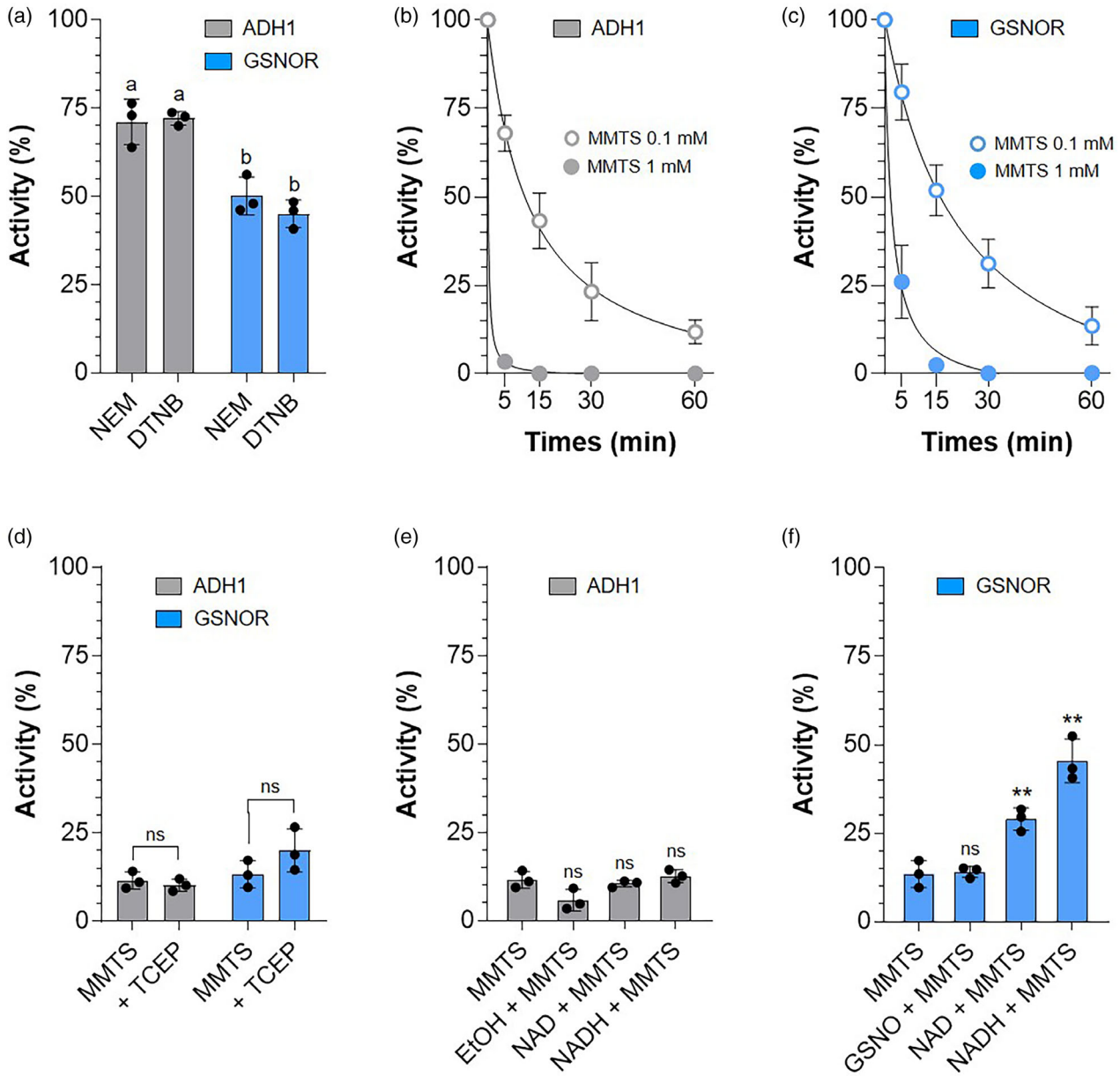

Figure 6. Sensitivity of Arabidopsis ADHs to thiol-modifying agents.
(a) Inactivation treatments of ADH1 (gray bars) and GSNOR (blue bars) with NEM or DTNB. Proteins (2 μM) were incubated for 60 min in the presence of 1 mM NEM or 0.2 mM DTNB. Data are represented as mean ± SD (n = 3).
(b, c) Inactivation treatments of ADH1 and GSNOR with MMTS. Proteins (2 μM) were incubated with 1 mM MMTS (closed gray/blue circles) or with 0.1 mM MMTS (open gray/blue circles). At the indicated times, an aliquot was withdrawn to measure enzyme activity. Data are represented as mean ± SD (n = 3).
(d, e) Substrate and cofactor protection of ADH1 (gray bars) and GSNOR (blue bars) from MMTS-dependent inactivation. Proteins were pre-incubated in the presence of cofactors (0.2 mM NAD(H)) or substrates (50 mM EtOH or 0.2 mM GSNO) and then exposed to 0.1 mM MMTS (1 h). Data are represented as mean ± SD (n = 3).
(f) The reversibility of ADH1 (gray bars) and GSNOR (blue bars) inactivation was assessed by the addition of 10 mM TCEP after 1 h incubation with 0.1 mM MMTS. Data are represented as mean ± SD (n = 3). For panels A–F, values are expressed as a percentage of protein activity measured under control conditions (see Experimental procedures). Statistical analysis was performed as described in Experimental procedures, *$P \leq 0.05$, **$P \leq 0.01$, ***$P \leq 0.001$, ****$P \leq 0.0001$, ns: not significant. Letters were used to distinguish groups that differ significantly.

thiol-modifying agents caused similar and partial inactivation of ADHs, which retained ~50% (GSNOR) and ~ 75% (ADH1) of control activity after a 60 min incubation. No further inhibition was observed at longer incubation times (~48% and~72% residual activity for ADH1 and GSNOR after 2 h of incubation, respectively). As DTNB forms reversible disulfide bonds, we assessed the recovery of enzyme activity in the presence of the strong reducing agent tris(2-carboxyethyl)phosphine (TCEP). Intriguingly, TCEP largely restored DTNB-dependent inactivation (~95 ± 2% and~90 ± 4% of maximal activity for ADH1 and GSNOR, respectively), indicating that for both ADHs the thiol-derivatization by DTNB does not involve metal-coordinating cysteines since the reduction of these eventually oxidized residues would not allow replenishment of the zinc ion and recovery of enzyme activity.

In total, these results indicate that DTNB/NEM-dependent protein inhibition is caused by derivatization of solvent-accessible cysteine residues other than the metal-coordinating cysteines. As the most likely candidates, we identified Cys271 in both enzymes, Cys243 in ADH1, and Cys370 in GSNOR. However, since the thiol group of these residues is poorly accessible in the enzyme structure we hypothesize that when DTNB or NEM approaches the cysteine residues, their side chains may rotate toward the protein surface making the thiol group available to react.

Arabidopsis ADH1 and GSNOR are both sensitive to the thiol-modifying agent MMTS

To further investigate the redox sensitivity of ADH1 and GSNOR, we examined the effect of the thiol-modifying agent MMTS, which can reversibly react with both accessible cysteines and metal-coordinating cysteine thiols (Tagliani et al., 2021). As shown in Figure 6b,c, both enzymes are highly sensitive, and exposure to 1 mM MMTS resulted in almost complete inhibition of enzyme activity after incubation for 5 min (ADH1) or 15 min (GSNOR). Inhibition kinetics were slower in the presence of 0.1 mM MMTS, but confirm the greater sensitivity of ADH1 compared with GSNOR (Figure 6b,c). We then evaluated the reversibility of protein inactivation and the protective effect of substrates (GSNO/EtOH) and cofactors (NAD/NADH) toward MMTS (0.1 mM) (Figure 6d–f). For both enzymes, TCEP was unable to restore enzyme activities (Figure 6d) and pre-incubation with substrates did not affect the extent of inactivation. Cofactors did not provide any protection for ADH1, while they were effective in decreasing MMTS-dependent inhibition of GSNOR (Figure 6e,f).

The strong and irreversible inhibitory effect of MMTS prompted us to investigate the impact on protein stability and folding by monitoring absorbance at 405 nm to measure changes in turbidity as an assay of protein misfolding and by analyzing secondary structure profiles using circular dichroism (CD). Surprisingly, MMTS caused dose-dependent GSNOR aggregation, with maximal turbidity reached after 1 h (1 mM) or 3 h (0.1 mM) (Figure S9). In contrast, no structural alteration was detected for ADH1 (Figure S10). Noticeably, CD analysis showed that MMTS (0.1 mM, 10:1 molar excess) does not alter the secondary structure of GSNOR significantly, while ADH1 appears to be slightly more sensitive (Figure S11 and Table S6).

Interference with zinc ion coordination and possible metal release was then examined using the PAR assay after exposure to 1 mM MMTS for 1 h. Each protein released ~1 zinc ion per monomer, the value being 1.08 ± 0.34 and 1.05 ± 0.13 for ADH1 and GSNOR, respectively.

Taken together, these results indicate that MMTS causes inhibition of both enzymes by altering the redox state of cysteine residues and particularly those involved in zinc ion coordination with consequent release of the metal. However, MMTS causes loss of structural integrity only for GSNOR.

H_2O_2-induced oxidation causes irreversible inhibition of ADH1 and GSNOR

Hydrogen peroxide (H_2O_2) is one of the most common reactive oxygen species (ROS) produced by plant cells in response to both normal and stress conditions, and it is known to primarily react with reactive cysteine thiols on proteins (Trost et al., 2017; Zaffagnini, Fermani, et al., 2019). To evaluate the propensity of ADH1 and GSNOR to undergo cysteine oxidation, we treated both proteins with 2 mM H_2O_2 and observed a decrease in enzymatic activities (Figure 7a). The time course of H_2O_2-mediated inhibition was much slower than that observed with MMTS, but again, ADH1 was more affected by H_2O_2 compared to GSNOR, retaining ~38% and~ 52% residual activity, respectively, after 1 h of incubation (Figure 7a). A longer incubation (4 h) had a more severe effect on both enzymes, causing almost complete inactivation (~2% and ~ 10% residual activity, respectively) (Figure 7a).

To determine if oxidation of ADH1 and GSNOR could be reversed by reducing treatments, we exploited two different reducing agents (TCEP and dithiothreitol, DTT) added independently to proteins partially inactivated by 1 h incubation with H_2O_2. Both reductants were ineffective in restoring protein activities indicating that H_2O_2 caused cysteine oxidation that irreversibly affects ADH1 and GSNOR functionality (Figure 7b). We then evaluated the protective effects of substrates and cofactors toward oxidation and examined the stability of protein folding and zinc ions coordination. Intriguingly, we observed no protection in the presence of their respective substrates (i.e., EtOH and GSNO for ADH1 and GSNOR, respectively), while oxidized or reduced cofactors strongly hindered the inhibitory effect of H_2O_2 with the inactivation of ADH1 almost completely abolished by the presence of NADH (Figure 7c,

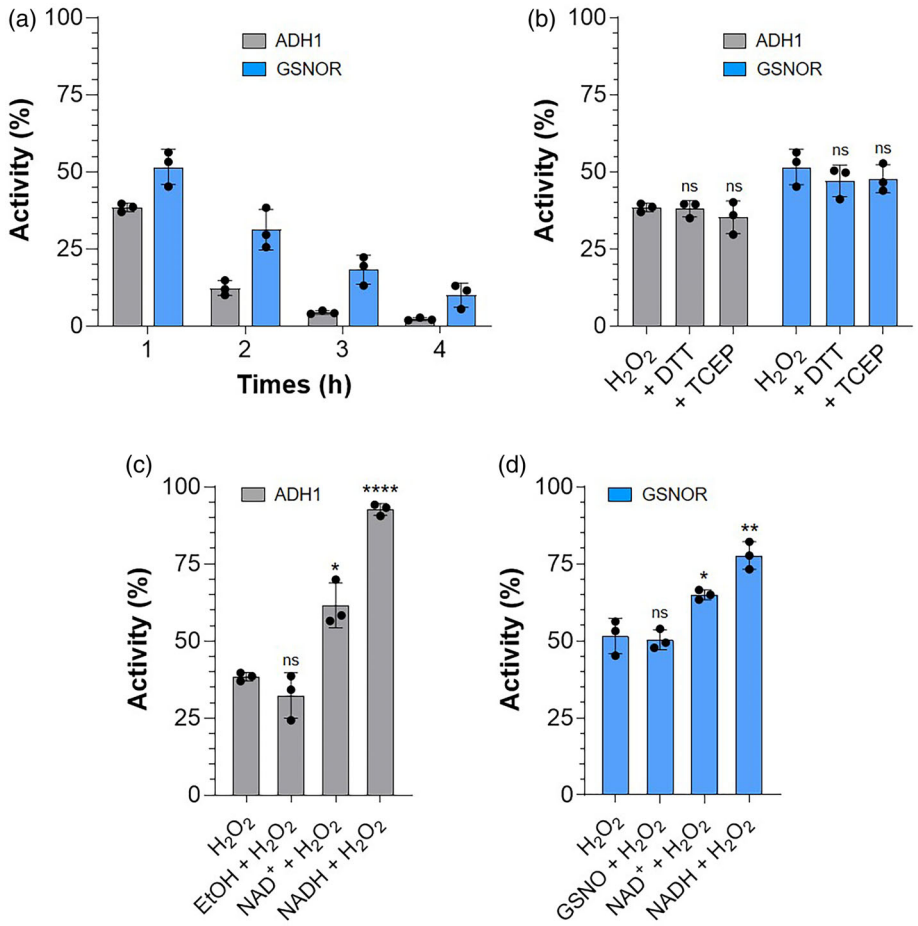

Figure 7. Sensitivity of Arabidopsis ADHs to H_2O_2-mediated oxidation.
(a) Inactivation treatments of ADH1 (gray bars) and GSNOR (blue bars) with H_2O_2. Proteins (2 μM) were incubated in the presence of 2 mM H_2O_2. At the indicated times, an aliquot was withdrawn to measure enzyme activity. Data are represented as mean ± SD (n = 3).
(b) The reversibility of ADH1 and GSNOR inactivation was assessed by incubating oxidized proteins (1 h incubation with 2 mM H_2O_2) with 10 mM TCEP or 20 mM DTT for 20 min after. Data are represented as mean ± SD (n = 3).
(c) and (d) Substrate and cofactor protection of ADH1 (gray bars) and GSNOR (blue bars) from H_2O_2-dependent inactivation. Proteins (2 μM) were pre-incubated with cofactors (0.2 mM NAD(H)) or substrates (50 mM EtOH or 0.2 mM GSNO) and then exposed to 2 mM H_2O_2 for 1 h. Data are represented as mean ± SD (n = 3). For panels A–D, values are expressed as a percentage of protein activity measured under control conditions (see Experimental procedures). Statistical analysis was performed as described in Experimental procedures, $*P \leq 0.05$, $**P \leq 0.01$, $***P \leq 0.001$, $****P \leq 0.0001$, ns: not significant.

d). As evidenced by the distortion of CD spectra, H_2O_2 treatment (2 mM, 200:1 molar excess) altered the secondary structure of both enzymes to similar extents (Figure S11 and Table S7). However, we observed no alteration in the structural stability for either protein (i.e., no turbidity increase) (Figures S9 and S10). Finally, we tested the possible interference of H_2O_2 on zinc ion coordination. Zinc ion release was determined after 4 h incubation with H_2O_2, and we found that ~1 zinc ion was released by each protein monomer (0.98 ± 0.07 and 0.92 ± 0.13 for ADH1 and GSNOR, respectively).

In total, these results indicate that exposure of Arabidopsis ADHs to H_2O_2 affects protein catalysis through oxidation of cysteine thiol(s) and destabilization of zinc coordination without altering native protein folding.

DISCUSSION

We report a detailed structural and biochemical comparison of ADH1 and GSNOR from *A. thaliana*. Despite their different physiological role, ADH1 and GSNOR have relatively high sequence identity and a similar 3D structure except for the conformation and dimension of the active site (Figures 3a,c,e and 5b,c; Figure S8). These localized structural differences could explain the stringent affinity of ADH1 and GSNOR toward their specific substrates (EtOH and GSNO, respectively) (Figure 5a). This is further reinforced by the presence of specific sequences in the active site that distinguish alcohol dehydrogenases capable to process ethanol from those that can degrade GSNO (Thr_{60}-Pro-(Leu/Val)$_{62}$ and Ser_{55}-Gly-(Lys/Ala)-Asp-Pro-Glu-Gly_{61}

sequences, respectively) (Figure S6) (Bui et al., 2019; Shafqat et al., 1996). Both enzymes, however, are capable of oxidizing long-chain alcohols, albeit with different proficiency (Figure 5d,e). GSNOR activity is significantly lower than ADH1 with octanol and cinnamyl alcohol, probably because its large catalytic cavity prevents efficient binding and orientation of these substrates. Accordingly, the catalytic efficiency of GSNOR slightly improves as substrate hindrance increases (from octanol to geraniol), while an opposite behavior is observed for ADH1. Both enzymes show the highest activity with the aromatic cinnamyl alcohol, possibly due to stabilizing interactions with aromatic residues located close to the catalytic zinc ion such as Phe95 (in ADH1) or Tyr95 (in GSNOR), Phe143 and Phe322 in both enzymes and Phe53 and Phe321 only in ADH1. However, we cannot exclude that besides active site size and configuration, additional factors participate in substrate binding and processing. In any case, these data reinforce the potential role of this class of enzymes in controlling the metabolism of alcohols/aldehydes in specific plant tissues as previously observed during fruit ripening and maturation (Kalua and Boss, 2009; Strommer, 2011).

We demonstrated that the activity of both ADH1 and GSNOR responds to thiol-modifying agents as previously reported (Dumont et al., 2018; Guerra et al., 2016; Kovacs et al., 2016; Ticha et al., 2017). DTNB-dependent thiol titration shows that both enzymes contain at least two solvent-accessible cysteine thiols, while ASA calculations indicate that in addition to some zinc-coordinating cysteines, also Cys243 in apo-ADH1, Cys370 in apo-GSNOR and Cys271 in both enzymes, are solvent-exposed (Table S5). When treated with the thiol-modifying agents NEM and DTNB, both enzymes undergo partial inactivation (Figure 6a), indicating that derivatization of solvent-accessible Cys thiols affects the catalytic activity of these enzymes. Among possible cysteine candidates, modified Cys271 could be responsible for the altered enzyme activity since it is located near the cofactor (Figure 4), and the modification of its thiol group (i.e., Cys-TNB disulfide or Cys-maleimide) could hinder proper cofactor binding. However, we cannot exclude that the reaction of DTNB/NEM with Cys243 in ADH1 and Cys370 in GSNOR may also contribute to the inactivation of the proteins. Unlike DTNB and NEM, MMTS and H_2O_2 led to a complete inactivation of the two enzymes, although with different inhibition kinetics (Figures 6 and 7). Previous studies reported that H_2O_2-dependent inactivation of plant GSNOR is reversed by treatment with the reducing agent DTT, whereas oxidative inactivation of plant ADH1 was not reversed by reducing treatments (Dumont et al., 2018; Kovacs et al., 2016). Our results show that inactivation is irreversible for both enzymes and associated with the release of one zinc ion, possibly the catalytic one. Consistently, both enzymes were previously identified as prominent targets of H_2O_2-induced oxidation in *A. thaliana* cell cultures, and Cys47 and Cys177, which coordinate the catalytic zinc ion, were identified as target sites (Huang, Willems, et al., 2019). Considering the protective effect of substrates/cofactors toward MMTS and H_2O_2 (Figures 6 and 7), we observed that protein substrates (i.e., EtOH and GSNO) were unable to limit the inhibitory effect, while cofactors, notably NADH, effectively counteracted thiol modification. Possible explanations for the protective mechanism of pyridine nucleotides reside in the fact that cofactor binding can directly protect accessible cysteine residues from modifications or induce conformational changes that may alter the protein sensitivity to thiol-modifying agents by changing the microenvironment and/or solvent accessibility of target cysteines. Notably, we observed that for both enzymes the interaction with oxidized or reduced cofactors affects the solvent accessibility of some cysteines including those involved in zinc ion coordination (Table S5).

In conclusion, our data reveal limited and localized structural differences in ADH1 and GSNOR catalytic sites that emphasize their stringent catalytic properties, and we show comparable redox sensitivity of the two enzymes. ADH1 and GSNOR play fundamental physiological roles in plant cells, being specifically involved in hypoxia-induced ethanolic fermentation and control of GSNO homeostasis, respectively (Jahnova et al., 2019; Lindermayr, 2017; Strommer, 2011). In the model plant *A. thaliana*, ADH1 and GSNOR are both encoded by a single gene and constitute the sole enzymes capable of catalyzing their respective reactions (NAD^+-dependent conversion of EtOH to MeCHO and NADH-dependent degradation of GSNO, respectively) (Bui et al., 2019; Lee et al., 2008; Xu et al., 2013). Having unique activities, regulation of ADH1 and GSNOR catalysis by thiol switching mechanisms becomes even more pivotal in controlling their physiological function, especially under stress conditions when plant cells experience an overproduction of ROS. In this regard, H_2O_2 is considered the most relevant oxidizing molecule within plant cells and here we demonstrated that both ADHs exhibit marked sensitivity to H_2O_2 with irreversible impairment of their activity (Figure 7). Likewise, altered nitric oxide (NO) homeostasis and treatment with NO donors have been shown to affect the activity of plant ADHs (Cheng et al., 2015; Dumont et al., 2018; Frungillo et al., 2014; Guerra et al., 2016; Zhan et al., 2018). Specifically, Arabidopsis ADHs are inhibited by S-nitrosylation, and Cys10, Cys271, and Cys370 have been identified as target residues for GSNOR (Guerra et al., 2016; Zhan et al., 2018). We can therefore postulate that various cysteine-based oxidative modifications (e.g., oxidation to sulfenic or sulfinic/sulfonic acids, S-nitrosylation, and likely S-glutathionylation) can modulate the function of both enzymes and potentially also impact their structural stability. In this regard, it will be crucial to identify cysteine residues that undergo redox modifications by analyzing

oxidized ADH forms through mass spectrometry and to assess their regulatory role by examining the redox sensitivity of single and/or multiple Cys mutants. What remains to be established is whether these thiol-switching mechanisms effectively occur their extent under physiological conditions, and with what type of stress or metabolic condition they are associated. Notably, redox-dependent inhibition of ADH activities might represent an important regulatory mechanism to control intracellular GSNO levels and activation of ethanol fermentation in response to hypoxic conditions, especially in *A. thaliana*, as both physiological pathways are specifically and uniquely controlled by GSNOR and ADH1.

EXPERIMENTAL PROCEDURES

Cloning, expression, and purification of *A. thaliana* ADH1 and GSNOR

The coding sequence for *A. thaliana* ADH1 (At1g77120) was amplified by standard RT-PCR on total Arabidopsis RNA extracts using a forward primer introducing a *Nde*I restriction site (in bold) at the start codon: 5′-GGCC**CATATG**TCTACCACCGGACAGAT-3′ and a reverse primer introducing a *Bam*HI restriction site (in bold) downstream of the stop codon: 5′-GGCC**CTCGAG**TCAAGCACCCATGGT GATGAT-3′. *ADH1* was then cloned in a pET-28a vector containing additional codons upstream of the *Nde*I site to express a tagged protein with six N-terminal histidines. The sequence was checked by sequencing. The pET-28a expression vector for *A. thaliana* GSNOR (At5g43940) was already available (Guerra et al., 2016). Both constructs were then used to transform *Escherichia coli* BL21 (DE3). Bacteria were grown in LB medium supplemented with 50 μg ml^{-1} kanamycin at 37°C and the production of both proteins was induced with 100 μM isopropyl β-D-1-thiogalactopyranoside overnight at 30°C. Cells were then harvested by centrifugation (5000 × ***g*** for 10 min) and resuspended in 30 mM Tris–HCl pH 7.9 (buffer A). Cell lysis was performed using a combination of lysozyme (100 μg per ml of cell suspension) and sonication (5 cycles of 2 min each) (Zaffagnini et al., 2014). Cell debris were removed by centrifugation (15 000 × ***g*** for 45 min) and the supernatant was applied onto a Ni^{2+}-Hitrap chelating resin (HIS-Select Nickel Affinity Gel; Sigma-Aldrich, Darmstadt, Germany) equilibrated with buffer A containing 500 mM NaCl and 5 mM imidazole. The recombinant ADH1 and GSNOR were further purified according to the manufacturer's instructions. The molecular mass and purity of each protein were examined by SDS-PAGE after desalting with PD-10 columns (GE Healthcare, Milan, Italy) equilibrated with buffer A. Protein concentration was determined spectrophotometrically using a molar extinction coefficient at 280 nm of 25 440 and 42 400 M^{-1} cm^{-1} for of ADH1 and GSNOR, respectively. The resulting homogeneous protein solutions were stored at −20°C.

Activity assays

The catalytic activity of both ADH1 and GSNOR was measured spectrophotometrically monitoring the NAD(H) reduction/oxidation at 340 nm. EtOH oxidation was measured in an assay mixture containing 50 mM glycine-NaOH (pH 9.8), 50 mM EtOH, and 2 mM NAD^+. GSNO-degrading activity was measured in a reaction buffer containing 100 mM Tris–HCl buffer (pH 7.9), 0.4 mM GSNO, and 0.2 mM NADH. For both proteins, the reaction was initiated by the addition of enzymes (10–50 nM) and activity was calculated using the linear variation of absorbance at 340 nm. To determine the pH optimum, the activity of both proteins was monitored as just described but using different pH buffers. The following buffers (50 mM) were used: potassium phosphate at pH 6.5–7.5; Tris–HCl at pH 7.5–9; and glycine at pH 9–10. Protein activities in the presence of long-chain alcohols (i.e., octanol, geraniol, and cinnamyl alcohol) were measured in a reaction mixture containing 50 mM glycine-NaOH (pH 9.8), 5 mM long-chain alcohols, 2 mM NAD^+, and variable amounts of ADH1 or GSNOR (50–400 nM).

DTNB-based thiol titration

The number of free cysteine thiols in as-purified and pre-reduced-ADHs was determined spectrophotometrically under non-denaturing conditions using 5,5′-dithiobis-2-nitrobenzoic acid (DTNB) (Zaffagnini et al., 2014; Zaffagnini, Fermani, et al., 2016). Pre-reduced proteins were obtained after 30 min incubation with 10 mM DTT following desalting with NAP-5 columns (GE-Healthcare) equilibrated with buffer A. ADHs were incubated at room temperature in 100 mM Tris–HCl (pH 7.9) supplemented with 0.2 mM DTNB. The formation of TNB^- was measured at 412 nm and the number of free thiols was calculated using a molar extinction coefficient of 14 150 M^{-1} cm^{-1}.

Cysteine-modifying treatments

Thiol-modifying treatments were performed by incubating ADHs (2 μM) in 50 mM Tris–HCl (pH 7.9) in the presence of 0.2 mM DTNB, or 1 mM NEM, or 0.1/1 mM MMTS, or 2 mM H_2O_2. Control incubations were carried out in the absence of thiol-modifying agents. At the indicated time points, an aliquot was withdrawn and enzymatic activities were assessed as described above. To assess the reversibility, treated proteins were incubated in the presence of 10 mM TCEP or DTT, and activities were measured after 30 min incubation. The protective effect of substrate(s) or cofactor(s) was carried out by pre-incubating ADH1 with 50 mM EtOH or 0.2 mM NAD(H), and GSNOR with 0.2 mM GSNO or 0.2 mM NAD(H). Residual activities were measured and expressed as a percentage of maximal activity (control conditions).

Zinc ion quantification

The zinc release was measured spectrophotometrically following the bathochromic shift of 4-(2-pyridylazo)resorcinol (PAR). Specifically, 2 μM of ADH1 or GSNOR were incubated in buffer A supplemented with 2 mM H_2O_2 for 4 h, or 1 mM MMTS for 1 h, or 2.5% SDS in the presence of 1 mM MMTS for 30 min. After incubation, PAR (15–40 μM) was added to ADH1 and GSNOR reaction mixtures, and the absorbance at 497 nM was monitored over time. Zinc ion released was calculated using a calibration curve with known quantities of $ZnCl_2$ as standards.

Turbidity measurements

The structural stability of ADHs was assayed spectrophotometrically by measuring the increase in absorbance at 405 nm (Zaffagnini, Marchand, et al., 2019). Proteins (2 μM) were incubated with 2 mM H_2O_2 or 0.1/1 mM MMTS and absorbance was monitored for 180 min using a Perkin Elmer VICTOR X3 MultiLabel Plate Reader.

Protein crystallization and data collection

Apo-GSNOR and NADH-ADH1 were crystallized using the hanging drop vapor diffusion method at 20°C. The drop was obtained by mixing 2 μl of 10 mg mL^{-1} (GSNOR) or 5 mg ml^{-1} (ADH1) protein solution both in buffer A supplemented with 1 mM EDTA, and an

equal volume of a reservoir solution containing 0.1 M Tris–HCl pH 8.5, 0.2 M $MgCl_2$, and 12–20% w/v PEG 4 K or 0.1 M Hepes-NaOH pH 7.0–8.0, 2% v/v PEG 400 and 2 M $(NH_4)_2SO_4$ for GSNOR and ADH1, respectively. Crystals with a rod-like (GSNOR) or rhombohedral (ADH1) morphology appeared after about 10 days. The crystals were fished, briefly soaked in a cryo-solution containing the reservoir components plus 20% v/v PEG 400 as cryoprotectant, and then frozen in liquid nitrogen. Diffraction data were collected at 100 K using the synchrotron radiation of the I03 beamline at Diamond (Oxford, UK) or XRD2 beamline at Elettra (Trieste, Italy) with a wavelength of 0.97 or 1.00 Å, a sample-to-detector distance of 217.02 (Eiger2 XE 16 M) or 311.29 mm (Pilatus 6 M), a beam size of 20 × 20 or 50 × 50 μm^2 and an exposition time of 0.08 or 0.1 sec for GSNOR and ADH1, respectively. An oscillation angle ($\Delta\varphi$) of 0.1° was used for all crystals. The images were indexed with XDS (Kabsch, 2010) and scaled with AIMLESS (Evans & Murshudov, 2013) from the CCP4 package (Winn et al., 2011). Data collection statistics are reported in Table S7.

Structure solution and refinement

Apo-GSNOR and NADH-ADH1 structures were solved by molecular replacement using the software PHASER (McCoy et al., 2007), and the coordinates of *A. thaliana* NAD^+-GSNOR (PDB ID 4JJI) and the AlphaFold (Jumper et al., 2021) model of *A. thaliana* ADH1 (AF-P06525) as search models, respectively. Two dimers and one monomer were placed in the asymmetric unit consistently with the calculated Matthews coefficient (Matthews, 1968) of 2.14 $Å^3$ Da^{-1} (solvent content 43%) for GSNOR and 2.48 $Å^3$ Da^{-1} (solvent content 50%) for ADH1. The initial electron density map of GSNOR showed that the cofactor was absent while an electron density compatible with NADH was clearly observed in ADH1. The refinement was performed with REFMAC 5.8.0135 (Murshudov et al., 2011) selecting 5% of reflections for R_{free}, and the manual rebuilding with Coot (Emsley & Cowtan, 2004). Water molecules were automatically added and, after a visual inspection, confirmed in the model only if contoured at 1.0 σ on the (2Fo − Fc) electron density map and they fell into an appropriate hydrogen-bonding environment. Several PEG molecules coming from the crystallization solution were identified and added to the model. The last refinement cycle was performed with PHENIX (Adams et al., 2010). Refinement statistics are reported in Table S7. The stereo-chemical quality of the models was checked with Molprobity (Chen et al., 2010). Molecular graphics images were generated using PyMOL (The PyMOL Molecular Graphics System, Schrödinger, LLC).

Structure analysis

The structural superposition and the subsequent RMSD calculations were conducted by using the Secondary Structure Matching algorithm in Coot (Emsley & Cowtan, 2004). The analysis of the protein cavity was performed using CAVER 3.0 (Chovancova et al., 2012) and CAVER Analyst 1.0 (Kozlikova et al., 2014) by setting the radius of the small and large probe spheres to 1.4 and 4.9 Å, respectively. The metal binding sites analysis and the pictures of the molecular structures were done using UCSF Chimera (Pettersen et al., 2004) and UCSF ChimeraX (Goddard et al., 2018; Pettersen et al., 2021). The ASA values were calculated by the software Areaimol from the CCP4 package (Winn et al., 2011).

Circular dichroism analysis

The secondary structures of ADHs were investigated by means of circular dichroism (CD) spectroscopy. Samples of both proteins (10 μM) were prepared in buffer A and quantified by spectrophotometric analysis at 280 nm in a 1-cm cell (ε_{280} = 25 440 M^{-1} cm^{-1} for ADH1 and 42 400 M^{-1} cm^{-1} for GSNOR) (Pace et al., 1995). Treated samples were obtained by incubating both proteins in the presence of 2 mM H_2O_2 (4 h) or 0.1 mM MMTS (1 h for GSNOR, 2 h for ADH1). The far-UV CD spectra (260–190 nm) of all samples were measured at room temperature on a J-715 spectropolarimeter (Jasco, Tokyo, Japan), using a QS-quartz cylindrical cell with 0.2 mm optical pathlength (Hellma Analytics, Müllheim, Germany), a 2 nm spectral bandwidth, a 50 nm/min scanning speed, a 2 sec data integration time, a 0.5 nm data interval and an accumulation cycle of 3 scans. The resulting CD spectra were corrected by subtracting the spectral contribution of solvent and eventual thiol-modifying agents, then converted to molar units per residue ($\Delta\varepsilon_{res}$, in M^{-1} cm^{-1}). The estimation of secondary structures from the CD spectra of native and treated samples was then performed using the CDSSTR algorithm (Sreerama & Woody, 2000) and the SP175 protein reference set (Lees et al., 2006) available on the DichroWeb web server (http://dichroweb.cryst.bbk.ac.uk/) (Miles et al., 2022).

Replicates and statistical analyses

All the results reported are representative of at least three independent biological replicates and expressed as mean ± SD. Statistical analysis was performed using an unpaired t-test with Welch's correction in the case of two categories or one-way ANOVA followed by a Tukey's post hoc test for multiple comparisons. *P* values reported on graphs as follows: $*P \leq 0.05$, $**P \leq 0.01$, $***P \leq 0.001$, $****P \leq 0.0001$. Letters were used to distinguish groups that differ significantly, as indicated in figure legends.

ACKNOWLEDGMENTS

We gratefully acknowledge Elettra (Trieste, Italy) and the European Synchrotron Radiation Facility (Grenoble, France) for allocation of beam time. SFermani and GF thank the Consorzio Interuniversitario di Ricerca in Chimica dei Metalli nei Sistemi Biologici (CIRCMSB). MM, JR, and SFanti are supported by a PhD grant from the University of Bologna (PhD programs in Cellular and Molecular Biology for MM and JR and in Nanoscience for Medicine and the Environment for SFanti). MZ is indebted to Dr. Amelie Lens for valuable and stimulating discussions. EV acknowledges support from the U.S. National Science Foundation, grant MCB 1817985. [Correction added on 19 March 2024, after first online publication: Prof. Vierling acknowledgement is inserted in this version.]

AUTHOR CONTRIBUTIONS

FM, SFermani, and MZ conceived and developed the experimental design. MM, JR, SFanti, GC, DT, FM, SFermani, and MZ performed the experiments and analyzed the data. MM, JR, DT, PTreffon, PTrost, EV, FL, BG, FM, SFermani, and MZ wrote, reviewed, and edited the manuscript. FM, SFermani, and MZ acquired funding and resource. All authors have read and agreed to the final version of the manuscript.

CONFLICT OF INTEREST

The authors have no conflicts of interest to declare.

DATA AVAILABILITY STATEMENT

Validated crystallographic reflection data and the model are deposited in the Protein Data Bank under identifiers 8CO4 and 8CON for apo-GSNOR and NADH-ADH1 structures, respectively.

SUPPORTING INFORMATION

Additional Supporting Information may be found in the online version of this article.

Figure S1. Sequence alignment of Arabidopsis ADHs. The alignment was performed as described in (Mattioli et al., 2022) using the sequence and structure of *Arabidopsis thaliana* ADH1 (PDB ID: 4RQU) and GSNOR (PDB ID: 4JJI). The conserved residues are shown in red background; blue boxes represent conserved amino acid stretches (>70%). Residues with similar physico-chemical properties are indicated in red. The following symbols '└' and '┘' were used to indicate the start and end of the catalytic domain (yellow) and the cofactor binding domain (dark red), respectively. α-helices, β-strands, and 310-helices are marked with α, β, and η, respectively. β-turns and α-turns are represented by TT and TTT, respectively. ADH1 and GSNOR share ~59% sequence identity and exhibit a nearly complete conservation of secondary structures except for a small α-helix (residues 117–120), a short β-strand (residues 304–306), and two β-turns (residues 300–301 and 368–369), found only in GSNOR.

Figure S2. Structural superposition of NAD^+-GSNOR monomers. Superposition of NAD^+ and the cofactor-binding site in GSNOR monomers (PDB ID 4JJI). Chain A (light blue) shows a nicotinamide moiety conformation similar to the structures of other available ADHs, while in chain B (wheat) the nicotinamide moiety is rotated about 90°. In addition, the loop Val295-Gln302, which is located at the entrance of the active site, has a different conformation in chain B with respect to chain A. The Protein chain is represented as cartoon, NAD^+ and residues as sticks, and the catalytic zinc ion as a sphere. The interactions between protein residues and NAD^+ of chain B are indicated and the corresponding distance values are reported in Table S4.

Figure S3. Coordination geometry of structural zinc ion in ADHs. Schemes of the coordination geometries of the structural zinc ions found in ADH1 and GSNOR crystal structures. The RMSD from the ideal geometry has been calculated using the UCSF Chimera 'Metal Geometry' tool. Legend to PDB IDs for ADH1: 4RQT, apo/acetate-form; 4RQU, NAD^+-form; 8CON, NADH-form. Legend to PDB IDs for GSNOR: 8CO4, apo-form; 4JJI, NAD^+-form; 3UKO, NADH-form. The letter indicates the structural chain.

Figure S4. Coordination geometry of catalytic zinc ion in ADHs. Schemes of the coordination geometries of the catalytic zinc ions found in ADH1 and GSNOR crystal structures. The RMSD from the ideal geometry has been calculated using the UCSF Chimera 'Metal Geometry' tool. Legend to PDB IDs for ADH1: 4RQT, apo/acetate-form; 4RQU, NAD^+-form; 8CON, NADH-form. Legend to PDB IDs for GSNOR: 8CO4, apo-form; 4JJI, NAD^+-form; 3UKO, NADH-form. The letter indicates the structural chain.

Figure S5. ADH1 and GSNOR structural superpositions. Superposition of ADH1 (a) and GSNOR (c) monomers. The protein backbone is reported as ribbon colored in blue, dark green, and salmon for apo-, NAD^+-, and NADH-structures, respectively. The cofactor and zinc ions are reported as sticks and spheres, respectively, colored with the same color scheme. RMSD values per residue obtained from the C_α atoms superposition of monomers of ADH1 (b) and GSNOR (d).

Figure S6. Sequence alignment to highlight cysteine conservation and catalytic-related residues in ADH1 and GSNOR. Conserved and unique cysteine residues are indicated by closed and open circles, respectively. The selection of residues found in the catalytic cavity of both ADH1 and GSNOR was based on their presence in the active site for more than 50% of the available structures (at least 3 for ADH1 and 5 for GSNOR). These residues are highlighted in bold and underlined. Non-conserved regions that delimit the entrance to the catalytic cavity and form the cavity itself (loops 55-69 and stretches 115-132 and 297-303) are indicated by closed triangles. The distinctive sequences in the active site for alcohol dehydrogenases capable to process ethanol (ADH1) or to degrade GSNO (GSNOR) are shown in gray (Bui et al., 2019). Residues involved in the binding of the catalytic and structural zinc ions are highlighted in yellow and cyan, respectively. The following symbols '└' and '┘' were used to indicate the start and end of the catalytic domain (yellow) and the cofactor binding domain (dark red), respectively.

Figure S7. Determination of pH optimum for ADH1 and GSNOR catalysis. (a) A plot of pH value versus the relative activity of ADH1 (gray bars). Values are represented as percentage of the maximal activity measured at pH 10. (b) A plot of pH value versus the relative activity of GSNOR (light blue bars). Values are represented as percentage of the maximal activity measured at pH 7.9. For both panels, data are represented as mean ± SD ($n = 3$).

Figure S8. Solvent excluded surface of the internal cavity calculated for ADH1 and GSNOR structures. Solvent-excluded surfaces of the catalytic cavities of ADH1 (top panel, gray) and GSNOR (bottom panel, light blue). The backbone of the protein is shown for reference as a thin ribbon. The catalytic zinc ion is represented by a purple sphere. The NAD^+/NADH cofactors have been removed in order to compare different structures. Legend to PDB IDs for ADH1: 4RQT, apo/acetate-form; 4RQU, NAD^+-form; 8CON, NADH-form. Legend to PDB IDs for GSNOR: 8CO4, apo-form; 4JJI, NAD^+-form; 3UKO, NADH-form. The letter indicates the structural chain.

Figure S9. Structural stability of GSNOR in response to thiol-modifying agents. (a) GSNOR was incubated up to 180 min under control conditions (control) or in the presence of 0.1 or 1 mM MMTS. (b) GSNOR was incubated as in panel A and the data are represented up to 60 min. (c) GSNOR was incubated up to 180 min in the presence of 1 mM NEM. (d) GSNOR was incubated up to 180 min in the presence of 2 mM H_2O_2. For all panels, protein stability was evaluated following the turbidity increase at 405 nm as a proxy of protein misfolding. Data are represented as the mean of three independent biological replicates ($n = 3$).

Figure S10. Structural stability of ADH1 in response to thiol-modifying agents. ADH1 was incubated for up to 180 min under control conditions (a, control), in the presence of 1 mM MMTS (b), 1 mM NEM (c), or 2 mM H_2O_2 (d). For all panels, protein stability was evaluated following the turbidity increase at 405 nm as a proxy of protein misfolding. Data are represented as the mean of three independent biological replicates ($n = 3$).

Figure S11. Circular dichroism (CD) spectra of ADH1 and GSNOR. (a) ADH1 (10 μM) before and after incubation with MMTS (0.1 mM) for 2 h. (b) ADH1 (10 μM) before and after incubation with H_2O_2 (2 mM) for 2 and 4 h. (c) GSNOR (10 μM) before and after incubation with MMTS (0.1 mM) for 1 h. (d) GSNOR (10 μM) before and after incubation with H_2O_2 (2 mM) for 2 and 4 h.

Table S1. Root mean square deviation (RMSD) values in Å were obtained from the superpositions of ADH1 and GSNOR monomers.

Table S2. Root mean square deviation (RMSD) values in Å were obtained from the superpositions of ADH1 and GSNOR dimers.

Table S3. Minimum, maximum, and average root mean square deviation (RMSD) values and standard deviations (SD) were obtained from the superpositions of ADH1 and GSNOR monomers and dimers.

Table S4. Hydrogen bond interactions between the cofactor (NAD^+ or NADH) and the protein residues in ADH structures. Residues in

bold, correspond to non-conserved amino acids between ADH1 and GSNOR. Only interactions at a distance ≤3.6 Å are considered.

Table S5. Accessibility surface area (ASA) values of cysteine residues and their Sγ atoms in ADHs structures. Cysteines highlighted in green and blue are those involved in the coordination of structural and catalytic zinc ions, respectively. The values in bold refer to the most accessible cysteines in the apo structures of both enzymes.

Table S6. Secondary structure estimations for ADH1 and GSNOR before and after treatment with MMTS or H_2O_2. Secondary structure estimations for ADH1 and GSNOR before and after treatment with MMTS or H_2O_2 (for details see Experimental procedures). Percentage values derived from analysis of CD spectra with DichroWeb (CDSSTR/SP175 method) (http://dichroweb.cryst.bbk.ac.uk/).

Table S7. Data collection and refinement statistics of ADHs structures.

REFERENCES

Achkor, H., Diaz, M., Fernandez, M.R., Biosca, J.A., Pares, X. & Martinez, M.C. (2003) Enhanced formaldehyde detoxification by overexpression of glutathione-dependent formaldehyde dehydrogenase from Arabidopsis. *Plant Physiology*, **132**, 2248–2255.

Adams, P.D., Afonine, P.V., Bunkoczi, G., Chen, V.B., Davis, I.W., Echols, N. *et al.* (2010) PHENIX: a comprehensive python-based system for macromolecular structure solution. *Acta Crystallographica. Section D, Biological Crystallography*, **66**, 213–221.

Antonio, C., Papke, C., Rocha, M., Diab, H., Limami, A.M., Obata, T. *et al.* (2016) Regulation of primary metabolism in response to low oxygen availability as revealed by carbon and nitrogen isotope redistribution. *Plant Physiology*, **170**, 43–56.

Broniowska, K.A., Diers, A.R. & Hogg, N. (2013) S-Nitrosoglutathione. *Biochimica et Biophysica Acta*, **1830**, 3173–3181.

Bui, L.T., Novi, G., Lombardi, L., Iannuzzi, C., Rossi, J., Santaniello, A. *et al.* (2019) Conservation of ethanol fermentation and its regulation in land plants. *Journal of Experimental Botany*, **70**, 1815–1827.

Chang, A., Jeske, L., Ulbrich, S., Hofmann, J., Koblitz, J., Schomburg, I. *et al.* (2021) BRENDA, the ELIXIR core data resource in 2021: new developments and updates. *Nucleic Acids Research*, **49**, D498–D508.

Chen, F., Wang, P., An, Y., Huang, J. & Xu, Y. (2015) Structural insight into the conformational change of alcohol dehydrogenase from *Arabidopsis thaliana* L. during coenzyme binding. *Biochimie*, **108**, 33–39.

Chen, V.B., Arendall, W.B., 3rd, Headd, J.J., Keedy, D.A., Immormino, R.M., Kapral, G.J. *et al.* (2010) MolProbity: all-atom structure validation for macromolecular crystallography. *Acta Crystallographica. Section D, Biological Crystallography*, **66**, 12–21.

Cheng, T., Chen, J., Ef, A.A., Wang, P., Wang, G., Hu, X. *et al.* (2015) Quantitative proteomics analysis reveals that S-nitrosoglutathione reductase (GSNOR) and nitric oxide signaling enhance poplar defense against chilling stress. *Planta*, **242**, 1361–1390.

Chovancova, E., Pavelka, A., Benes, P., Strnad, O., Brezovsky, J., Kozlikova, B. *et al.* (2012) CAVER 3.0: a tool for the analysis of transport pathways in dynamic protein structures. *PLoS Computational Biology*, **8**, e1002708.

Dixon, D.P., Skipsey, M., Grundy, N.M. & Edwards, R. (2005) Stress-induced protein S-glutathionylation in *Arabidopsis*. *Plant Physiology*, **138**, 2233–2244.

Dumont, S., Bykova, N.V., Khaou, A., Besserour, Y., Dorval, M. & Rivoal, J. (2018) *Arabidopsis thaliana* alcohol dehydrogenase is differently affected by several redox modifications. *PLoS One*, **13**, e0204530.

Dupuis, J.H., Wang, S., Song, C. & Yada, R.Y. (2020) The role of disulfide bonds in a Solanum tuberosum saposin-like protein investigated using molecular dynamics. *PLoS One*, **15**, e0237884.

Emsley, P. & Cowtan, K. (2004) Coot: model-building tools for molecular graphics. *Acta Crystallographica. Section D, Biological Crystallography*, **60**, 2126–2132.

Evans, P.R. & Murshudov, G.N. (2013) How good are my data and what is the resolution? *Acta Crystallographica. Section D, Biological Crystallography*, **69**, 1204–1214.

Fares, A., Rossignol, M. & Peltier, J.B. (2011) Proteomics investigation of endogenous S-nitrosylation in Arabidopsis. *Biochemical and Biophysical Research Communications*, **416**, 331–336.

Fliegmann, J. & Sandermann, H., Jr. (1997) Maize glutathione-dependent formaldehyde dehydrogenase cDNA: a novel plant gene of detoxification. *Plant Molecular Biology*, **34**, 843–854.

Frungillo, L., Skelly, M.J., Loake, G.J., Spoel, S.H. & Salgado, I. (2014) S-nitrosothiols regulate nitric oxide production and storage in plants through the nitrogen assimilation pathway. *Nature Communications*, **5**, 5401.

Goddard, T.D., Huang, C.C., Meng, E.C., Pettersen, E.F., Couch, G.S., Morris, J.H. *et al.* (2018) UCSF ChimeraX: meeting modern challenges in visualization and analysis. *Protein Science*, **27**, 14–25.

Guerra, D., Ballard, K., Truebridge, I. & Vierling, E. (2016) S-Nitrosation of conserved cysteines modulates activity and stability of S-Nitrosoglutathione reductase (GSNOR). *Biochemistry*, **55**, 2452–2464.

Huang, D., Huo, J., Zhang, J., Wang, C., Wang, B., Fang, H. *et al.* (2019) Protein S-nitrosylation in programmed cell death in plants. *Cellular and Molecular Life Sciences*, **76**, 1877–1887.

Huang, J., Willems, P., Wei, B., Tian, C., Ferreira, R.B., Bodra, N. *et al.* (2019) Mining for protein S-sulfenylation in Arabidopsis uncovers redox-sensitive sites. *Proceedings of the National Academy of Sciences of the United States of America*, **116**, 21256–21261.

Jahnova, J., Luhova, L. & Petrivalsky, M. (2019) S-Nitrosoglutathione reductase-the master regulator of protein S-Nitrosation in plant NO signaling. *Plants (Basel)*, **8**, 48.

Jumper, J., Evans, R., Pritzel, A., Green, T., Figurnov, M., Ronneberger, O. *et al.* (2021) Highly accurate protein structure prediction with AlphaFold. *Nature*, **596**, 583–589.

Kabsch, W. (2010) Xds. *Acta Crystallographica. Section D, Biological Crystallography*, **66**, 125–132.

Kalua, C.M. & Boss, P.K. (2009). Evolution of volatile compounds during the development of cabernet sauvignon grapes (Vitis vinifera L.). *Journal of Agricultural and Food Chemistry*, **57**, 3818–3830. https://doi.org/10.1021/jf803471n

Kovacs, I., Holzmeister, C., Wirtz, M., Geerlof, A., Frohlich, T., Romling, G. *et al.* (2016) ROS-mediated inhibition of S-nitrosoglutathione reductase contributes to the activation of anti-oxidative mechanisms. *Frontiers in Plant Science*, **7**, 1669.

Kozlikova, B., Sebestova, E., Sustr, V., Brezovsky, J., Strnad, O., Daniel, L. *et al.* (2014) CAVER analyst 1.0: graphic tool for interactive visualization and analysis of tunnels and channels in protein structures. *Bioinformatics*, **30**, 2684–2685.

Krzywoszynska, K., Swiatek-Kozlowska, J., Potocki, S., Ostrowska, M. & Kozlowski, H. (2020) Triplet of cysteines—Coordinational riddle? *Journal of Inorganic Biochemistry*, **204**, 110957.

Kubienova, L., Kopecny, D., Tylichova, M., Briozzo, P., Skopalova, J., Sebela, M. *et al.* (2013) Structural and functional characterization of a plant S-nitrosoglutathione reductase from Solanum lycopersicum. *Biochimie*, **95**, 889–902.

Lee, U., Wie, C., Fernandez, B.O., Feelisch, M. & Vierling, E. (2008) Modulation of nitrosative stress by S-nitrosoglutathione reductase is critical for thermotolerance and plant growth in Arabidopsis. *Plant Cell*, **20**, 786–802.

Lees, J.G., Miles, A.J., Wien, F. & Wallace, B.A. (2006) A reference database for circular dichroism spectroscopy covering fold and secondary structure space. *Bioinformatics*, **22**, 1955–1962.

Lindermayr, C. (2017) Crosstalk between reactive oxygen species and nitric oxide in plants: key role of S-nitrosoglutathione reductase. *Free Radical Biology and Medicine*, **122**, 110–115.

Liu, L., Hausladen, A., Zeng, M., Que, L., Heitman, J. & Stamler, J.S. (2001) A metabolic enzyme for S-nitrosothiol conserved from bacteria to humans. *Nature*, **410**, 490–494.

Loreti, E., van Veen, H. & Perata, P. (2016) Plant responses to flooding stress. *Current Opinion in Plant Biology*, **33**, 64–71.

Marshall, R.S., Frigerio, L. & Roberts, L.M. (2010) Disulfide formation in plant storage vacuoles permits assembly of a multimeric lectin. *The Biochemical Journal*, **427**, 513–521.

Matthews, B.W. (1968) Solvent content of protein crystals. *Journal of Molecular Biology*, **33**, 491–497.

Mattioli, E.J., Rossi, J., Meloni, M., De Mia, M., Marchand, C.H., Tagliani, A. *et al.* (2022) Structural snapshots of nitrosoglutathione binding and

reactivity underlying S-nitrosylation of photosynthetic GAPDH. *Redox Biology*, **54**, 102387.

McCoy, A.J., **Grosse-Kunstleve, R.W.**, **Adams, P.D.**, **Winn, M.D.**, **Storoni, L.C.** & **Read, R.J.** (2007) Phaser crystallographic software. *Journal of Applied Crystallography*, **40**, 658–674.

Miles, A.J., **Ramalli, S.G.** & **Wallace, B.A.** (2022) DichroWeb, a website for calculating protein secondary structure from circular dichroism spectroscopic data. *Protein Science*, **31**, 37–46.

Murshudov, G.N., **Skubak, P.**, **Lebedev, A.A.**, **Pannu, N.S.**, **Steiner, R.A.**, **Nicholls, R.A.** ***et al.*** (2011) REFMAC5 for the refinement of macromolecular crystal structures. *Acta Crystallographica. Section D, Biological Crystallography*, **67**, 355–367.

Orengo, C.A., **Michie, A.D.**, **Jones, S.**, **Jones, D.T.**, **Swindells, M.B.** & **Thornton, J.M.** (1997) CATH – a hierarchic classification of protein domain structures. *Structure*, **5**, 1093–1108.

Pace, C.N., **Vajdos, F.**, **Fee, L.**, **Grimsley, G.** & **Gray, T.** (1995) How to measure and predict the molar absorption coefficient of a protein. *Protein Science*, **4**, 2411–2423.

Pace, N.J. & **Weerapana, E.** (2014) Zinc-binding cysteines: diverse functions and structural motifs. *Biomolecules*, **4**, 419–434.

Paulsen, C.E. & **Carroll, K.S.** (2013) Cysteine-mediated redox signaling: chemistry, biology, and tools for discovery. *Chemical Reviews*, **113**, 4633–4679.

Permyakov, E.A. (2021) Metal binding. *Proteins*, **1**, 261–292.

Persson, B., **Hedlund, J.** & **Jornvall, H.** (2008) Medium- and short-chain dehydrogenase/reductase gene and protein families: the MDR superfamily. *Cellular and Molecular Life Sciences*, **65**, 3879–3894.

Pettersen, E.F., **Goddard, T.D.**, **Huang, C.C.**, **Couch, G.S.**, **Greenblatt, D.M.**, **Meng, E.C.** ***et al.*** (2004) UCSF chimera—a visualization system for exploratory research and analysis. *Journal of Computational Chemistry*, **25**, 1605–1612.

Pettersen, E.F., **Goddard, T.D.**, **Huang, C.C.**, **Meng, E.C.**, **Couch, G.S.**, **Croll, T.I.** ***et al.*** (2021) UCSF ChimeraX: structure visualization for researchers, educators, and developers. *Protein Science*, **30**, 70–82.

Poole, L.B. (2015) The basics of thiols and cysteines in redox biology and chemistry. *Free Radical Biology & Medicine*, **80**, 148–157.

Shafqat, J., **El-Ahmad, M.**, **Danielsson, O.**, **Martinez, M.C.**, **Persson, B.**, **Pares, X.** ***et al.*** (1996) Pea formaldehyde-active class III alcohol dehydrogenase: common derivation of the plant and animal forms but not of the corresponding ethanol-active forms (classes I and P). *Proceedings of the National Academy of Sciences of the United States of America*, **93**, 5595–5599.

Sreerama, N. & **Woody, R.W.** (2000) Estimation of protein secondary structure from circular dichroism spectra: comparison of CONTIN, SELCON, and CDSSTR methods with an expanded reference set. *Analytical Biochemistry*, **287**, 252–260.

Strommer, J. (2011) The plant ADH gene family. *The Plant Journal*, **66**, 128–142.

Tagliani, A., **Rossi, J.**, **Marchand, C.H.**, **De Mia, M.**, **Tedesco, D.**, **Gurrieri, L.** ***et al.*** (2021) Structural and functional insights into nitrosoglutathione reductase from Chlamydomonas reinhardtii. *Redox Biology*, **38**, 101806.

Ticha, T., **Lochman, J.**, **Cincalova, L.**, **Luhova, L.** & **Petrivalsky, M.** (2017) Redox regulation of plant S-nitrosoglutathione reductase activity through post-translational modifications of cysteine residues. *Biochemical and Biophysical Research Communications*, **494**, 27–33.

Trivedi, M.V., **Laurence, J.S.** & **Siahaan, T.J.** (2009) The role of thiols and disulfides on protein stability. *Current Protein & Peptide Science*, **10**, 614–625.

Trost, P., **Fermani, S.**, **Calvaresi, M.** & **Zaffagnini, M.** (2017) Biochemical basis of sulphenomics: how protein sulphenic acids may be stabilized by the protein microenvironment. *Plant, Cell & Environment*, **40**, 483–490.

Wei, B., **Willems, P.**, **Huang, J.**, **Tian, C.**, **Yang, J.**, **Messens, J.** ***et al.*** (2020) Identification of Sulfenylated cysteines in *Arabidopsis thaliana* proteins using a disulfide-linked peptide reporter. *Frontiers in Plant Science*, **11**, 777.

Winn, M.D., **Ballard, C.C.**, **Cowtan, K.D.**, **Dodson, E.J.**, **Emsley, P.**, **Evans, P.R.** ***et al.*** (2011) Overview of the CCP4 suite and current developments. *Acta Crystallographica. Section D, Biological Crystallography*, **67**, 235–242.

Xu, S., **Guerra, D.**, **Lee, U.** & **Vierling, E.** (2013) S-nitrosoglutathione reductases are low-copy number, cysteine-rich proteins in plants that control multiple developmental and defense responses in Arabidopsis. *Frontiers in Plant Science*, **4**, 430.

Yamazaki, D., **Motohashi, K.**, **Kasama, T.**, **Hara, Y.** & **Hisabori, T.** (2004) Target proteins of the cytosolic thioredoxins in *Arabidopsis thaliana*. *Plant & Cell Physiology*, **45**, 18–27.

Zaffagnini, M., **De Mia, M.**, **Morisse, S.**, **Di Giacinto, N.**, **Marchand, C.H.**, **Maes, A.** ***et al.*** (2016) Protein S-nitrosylation in photosynthetic organisms: a comprehensive overview with future perspectives. *Biochimica et Biophysica Acta*, **1864**, 952–966.

Zaffagnini, M., **Fermani, S.**, **Calvaresi, M.**, **Orru, R.**, **Iommarini, L.**, **Sparla, F.** ***et al.*** (2016) Tuning cysteine reactivity and sulfenic acid stability by protein microenvironment in Glyceraldehyde-3-phosphate dehydrogenases of *Arabidopsis thaliana*. *Antioxidants & Redox Signaling*, **24**, 502–517.

Zaffagnini, M., **Fermani, S.**, **Marchand, C.H.**, **Costa, A.**, **Sparla, F.**, **Rouhier, N.** ***et al.*** (2019) Redox homeostasis in photosynthetic organisms: novel and established thiol-based molecular mechanisms. *Antioxidants & Redox Signaling*, **31**, 155–210.

Zaffagnini, M., **Marchand, C.H.**, **Malferrari, M.**, **Murail, S.**, **Bonacchi, S.**, **Genovese, D.** ***et al.*** (2019) Glutathionylation primes soluble glyceraldehyde-3-phosphate dehydrogenase for late collapse into insoluble aggregates. *Proceedings of the National Academy of Sciences of the United States of America*, **116**, 26057–26065.

Zaffagnini, M., **Michelet, L.**, **Sciabolini, C.**, **Di Giacinto, N.**, **Morisse, S.**, **Marchand, C.H.** ***et al.*** (2014) High-resolution crystal structure and redox properties of chloroplastic triosephosphate isomerase from Chlamydomonas reinhardtii. *Molecular Plant*, **7**, 101–120.

Zhan, N., **Wang, C.**, **Chen, L.**, **Yang, H.**, **Feng, J.**, **Gong, X.** ***et al.*** (2018) S-Nitrosylation targets GSNO reductase for selective autophagy during hypoxia responses in plants. *Molecular Cell*, **71**, 142–154.e6.

Zhang, T., **Ma, M.**, **Chen, T.**, **Zhang, L.**, **Fan, L.**, **Zhang, W.** ***et al.*** (2020) Glutathione-dependent denitrosation of GSNOR1 promotes oxidative signalling downstream of H_2O_2. *Plant, Cell & Environment*, **43**, 1175–1191.